MAGNETOHYDRODYNAMIC TURBULENCE

Thesis by

Jason Maron

In Partial Fulfillment of the Requirements
for the Degree of
Doctor of Philosophy

California Institute of Technology
Pasadena, California

2001
(Submitted September 19, 2000)

© 2001
Jason Maron
All Rights Reserved

Abstract

We simulate incompressible, MHD turbulence using a pseudo-spectral code. Our major conclusions are as follows.

1) MHD turbulence is most conveniently described in terms of counter propagating shear Alfvén and slow waves. Shear Alfvén waves control the cascade dynamics. Slow waves play a passive role and adopt the spectrum set by the shear Alfvén waves. Cascades composed entirely of shear Alfvén waves do not generate a significant measure of slow waves.

2) MHD turbulence is anisotropic with energy cascading more rapidly along $k_\perp$ than along $k_{||}$, where $k_\perp$ and $k_{||}$ refer to wavevector components perpendicular and parallel to the local magnetic field. Anisotropy increases with increasing $k_\perp$ such that excited modes are confined inside a cone bounded by $k_{||} \propto k_\perp^\gamma$ where $\gamma < 1$. The opening angle of the cone, $\theta(k_\perp) \propto k_\perp^{-(1-\gamma)}$, defines the scale dependent anisotropy.

3) MHD turbulence is generically strong in the sense that the waves which comprise it suffer order unity distortions on timescales comparable to their periods. Nevertheless, turbulent fluctuations are small deep inside the inertial range. Their energy density is less than that of the background field by a factor $\theta^2(k_\perp) \ll 1$.

4) MHD cascades are best understood geometrically. Wave packets suffer distortions as they move along magnetic field lines perturbed by counter propagating waves. Field lines perturbed by unidirectional waves map planes perpendicular to the local field into each other. Shear Alfvén waves are responsible for the mapping's shear and slow waves for its dilatation. The amplitude of the former exceeds that of the latter by $1/\theta(k_\perp)$ which accounts for dominance of the shear Alfvén waves in controlling the cascade dynamics.

5) Passive scalars mixed by MHD turbulence adopt the same power spectrum as the velocity and magnetic field perturbations.

6) Decaying MHD turbulence is unstable to an increase of the imbalance between

the flux of waves propagating in opposite directions along the magnetic field. Forced MHD turbulence displays order unity fluctuations with respect to the balanced state if excited at low k by $\delta(t)$ correlated forcing. It appears to be statistically stable to the unlimited growth of imbalance.

7) Gradients of the dynamic variables are focused into sheets aligned with the magnetic field whose thickness is comparable to the dissipation scale. Sheets formed by oppositely directed waves are uncorrelated. We suspect that these are vortex sheets which the mean magnetic field prevents from rolling up.

8) Items (1)-(5) lend support to the model of strong MHD turbulence put forth by Goldreich and Sridhar (1995, 1997). Results from our simulations are also consistent with the GS prediction $\gamma = 2/3$. The sole notable discrepancy is that the 1D power law spectra, $E(k_\perp) \propto k_\perp^{-\alpha}$, determined from our simulations exhibit $\alpha \approx 3/2$, whereas the GS model predicts $\alpha = 5/3$.

Contents

List of Figures

Chapter 1 INTRODUCTION

1.1 Galactic Turbulence

The galaxy is host to varied environments where turbulence plays a role. This work is concerned with the specialized case of small-scale MHD turbulence, where the energy in the uniform component of the magnetic field outweighes that in the fluctuations. This regime has the character of strongly-interacting Alfvén waves. In establishing the astrophysical context of this regime, we give an overview of the structure of the interstellar medium (ISM) with the principal sources of turbulence. We also discuss implications of Alfvén wave turbulence for various astrophysical phenomena.

1.1.1 ISM

We identify four representative phases of the interstellar medium (ISM) and assign a set of example values to each (Spitzer 1978, Heiles 2000).

Phase	n_H	n_e	T	$b_{\rm rms}$	v_S	v_A
Cloud	> 1000	> 0.01	30	$> 3 \cdot 10^{-4}$	$> 5 \cdot 10^4$	10^6
Cold	1	10^{-5}	80	$3 \cdot 10^{-6}$	10^5	10^6
Warm	0.01	0.01	8000	$3 \cdot 10^{-7}$	10^6	10^6
Hot	0.003	0.003	10^6	10^{-7}	10^7	10^6

n_H and n_e are the number densities of hydrogen (or protons, if ionized) and free electrons. The ratio of acoustic (v_S) to Alfvén (v_A) speeds can be larger or smaller than unity. Formally v_S is infinite in our simulations, however the Alfvén wave cascade results require only that the Alfvén speed substantially exceed that of the fluctuations.

The warm phase, alternatively known as the diffuse ionized gas (DIG) or the warm ionized medium (WIM), is generally associated with ionizing stars. The hot phase is

associated with supernova remnants and superbubbles, and tends to dominate in the Galactic corona more than 100 pc from the disk midplane. The cloud phase consists of gravitationally condensed matter and is host to star-forming activity.

For calculations of turbulent intensities, we assume an outer scale velocity of $v_> \sim 10$ km/s, a lengthscale of $L_> \sim 10$ pc, a density of $n_H \sim 1\text{cm}^{-3}$, and a Galactic ISM mass of $10^{10}\ M_\odot$, which implies a turbulent dissipation rate of $\sim 3 \cdot 10^{41}\text{ergs}^{-1}$. It falls upon us to identify the principal sources of turbulence which can supply this power.

1.1.2 Sources of Turbulence

Supernovae, which occur every $\sim$ 30 years, inject $\sim 10^{51}$ ergs of energy into the ISM. As the supernova ejecta expands, some fraction of the energy ($\sim 4\%$) (Dyson & Williams 1987) drives kinetic motion in the surrounding ISM, with the rest going into heat (which is subsequently radiated) and the production of cosmic rays. The turbulent energy input associated with supernovae is therefore $\sim 3 \cdot 10^{40}$ erg/s. This is the principal origin of the hot coronal gas.

Massive O stars contribute energy to the interstellar medium through winds and the expansion of ionization fronts. The winds tend to have velocities of $\sim$ 2000 km/s and a mass flux of $\sim 10^{-6} M_\odot \text{yr}^{-1}$, implying a mechanical energy output of 10^{36} erg/s. There are $\sim$ 20,000 O stars (Mathis 1986, ApJ301,423), giving an energy of $2 \cdot 10^{40}$ erg/s.

High velocity clouds (HVC) consist of HI and have Doppler velocities placing them out of the Galactic rotation curve (Wakker & Woerden 1997). Their probable origin is from supernova fountains ($5 M_\odot\ yr^{-1}$) and accretion ($1 M_\odot\ yr^{-1}$). Assuming an infall velocity of 200 km/s, accretion represents an energy input rate of 10^{40} erg/s. In a simulation of a cloud-disk collision, MacLow et al. (1989) obtained a resulting temperature of 10^5 K, suggesting that they are not responsible for the hot ionized medium.

1.2 Applications

1.2.1 Scintillation

ISM turbulence is indirectly observable through interstellar scintillation (ISS). The free electron density n_e constitutes a spatially-varying index of refraction responsible for the scintillation of pulsar radio sources. We consider a scenario where fluctuations in entropy, and hence n_e, exist in pressure equilibrium and evolve as a passive scalar. The turbulent dynamics therefore determine the spectrum of n_e fluctuations.

The scattering measure is defined by $\mathrm{SM} = \int C_n^2(z)dz$, where the electron density spectrum is given by $E_{n_e}(k,z) = C_n^2(z)k^{-\alpha}$ and z is the path from the source to the observer. Assuming a Kolmogorov form and an outer scale $\lambda_>$, we have $C_n^2 \sim n_e^2 \lambda_>^{-2/3}$.

Armstrong, Rickett, & Spangler (1995) summarize our knowledge of turbulence obtained from various pulsar lines of sight. Information about the smallest scales (10^9cm) comes from diffractive scintillation, angular broadening, and decorrelation bandwidth observations. Refractive scintillation and dispersion measure fluctuations probe structure at scales of $\sim 10^{14}$ cm. Rotation measure and direct angle-resolved observations cover the outer scale conditions at $\sim 10^{19}$ cm. By splicing together information at each scale, they obtain an averaged spectrum with $C_n^2 \sim 5 \cdot 10^{-17}\mathrm{cm}^{-20/3}$, and a power law index consistent with a uniform value of 5/3 throughout the 11 decades of range. The uniformity of the index plus the fact that it is smaller than 2 suggests a turbulent process. They identify the WIM as the dominant source of scintillation. Using a value of $n_e \sim 10^{-2}$ from dispersion measure observations, we have an outer scale of $\lambda_> \sim 3 \cdot 10^{18}$. They also place an upper bound on the inner scale of 10^{10} cm and mention that much smaller values can exist on the most active lines of sight.

Observations of anisotropic scattering (Molnar et al. 1995, Spangler & Cordes 1998) suggest an origin in anisotropic electron density fluctuations.

1.2.2 Heating

The Alfvén wave cascade experiences a transition at the ion cyclotron scale where MHD breaks down. From there, the energy can either go into ion thermal motion or it can continue into an electron hydrodynamic cascade which ultimately heats electrons. The question of which species is heated is of interest to accretion onto compact objects, where the temperature is sufficiently high that the collision length exceeds the system size, and therefore energy is not exchanged between protons and electrons. The advection dominated accretion flow (ADAF) model assumes that ions are preferentially heated, which are then accreted spherically before they can radiate their energy. If electrons are heated, they can radiate before accreting.

Quataert and Gruzinov (1998) found that the issue depends critically on the anisotropy and rate of the cascade. Wave-particle resonances occur when $k_{||}(u_{||}-v_A) = n\Omega_{cy}$ where $\uparrow$ is the particle velocity, $\mathbf{k}$ is the wavevector, and Ω_{cy} is the cyclotron frequency. Particles are accelerated by $E_{||}$ for Landau damping and $b_{||}$ for transit time damping (TTD). Both $E_{||}$ and $b_{||}$ are zero for Alfvén waves until the proton cyclotron scale is reached, where particle effects become important. Therefore, particle damping is only significant in the range of the cyclotron radius. For anisotropic turbulence with $\beta \geq 1$ there are negligibly few particles fast enough to satisfy the $n \neq 0$ resonances. For the $n = 0$ resonance, TTD damping increases with β because the protons have a higher magnetic moment for interacting with $b_{||}$. The amount of energy damped by the protons depends on how quickly the cascade proceeds through the cyclotron range. Drawing from results in this thesis for the energy cascade rate, Quataert and Gruzinov found that the division between proton and electron heating occurs somewhere between $\beta \sim 5$ and $\beta \sim 100$. Larger β results in the protons being heated and smaller β results in the electrons being heated.

1.2.3 Cosmic Ray Scattering

Cosmic rays are scattered by Alfvén waves, and they can also generate Alfvén waves (Kulsrud & Pearce 1969, Blandford & Eichler 1987). Chandran (2000) found that

the anisotropic structure of GS turbulence suppresses scattering. The results can be summarized as follows. Particles resonate with Alfvén waves when $k_{||}(u_{||} - v_A) = n\Omega_{cy} = nu_{\perp}/(2\pi r_{cy})$, where $\uparrow$ is the cosmic ray velocity, $\mathbf{k}$ is the wavevector, Ω_{cy} is the cyclotron frequency, and r_{cy} is the cyclotron radius. For $u_{\perp} \sim u_{||}$, $r_{cy} \sim \lambda_{||} << \lambda_{\perp}$. The cosmic ray samples many incoherent transverse wavemodes per orbit and the scattering is weak. Alfvén wave scattering is strong when the pitch angle θ is less than $\lambda_{\perp}/\lambda_{||}$, where then $r_{cy} < \lambda_{\perp}$. Strong scattering from slow modes is possible when $v_{||} = v_A$, which occurs when $\theta \sim \pi/2$. The resonance condition also implies that wavemodes excited by cosmic rays have $k_{\perp} \sim k_{||}$. These modes interact weakly with the anisotropic modes.

1.2.4 Particle Transport

Chandran & Cowley (1998) calculated plasma conductivities with application to intragalactic cooling flows in situations where the collision length exceeds the magnetic coherence length. In their model, magnetic structure enters the picture through the divergence of neighboring fieldlines and the trapping of electrons by magnetic mirrors. Electrons are confined to fieldlines until they change directions through scattering or mirroring, at which point they can become displaced onto a new fieldline separated from the original fieldline by of order the cyclotron radius. The departure of the electron from its original trajectory and its subsequent transport is then determined by the divergence of the old and new fieldlines from each other.

The Rosenbluth scaling for the divergence of fieldlines derives from the assumption of isotropic turbulence and states that $\Delta r \sim r_0 e^{z/z_0}$, where r_0 is the initial fieldline spearation, z is the path along the fieldline, z_0 is a scale length, and Δr is the characteristic fieldline separation at z. The appropriate scalings for anisotropic Alfvén turbulence are:

$$\text{Strong regime}: \quad \Delta r = J_S \epsilon^{1/2} v_A^{-3/2} z^{3/2}$$

$$\text{Intermediate regime}: \quad \Delta r = J_I \frac{v_F^{3/2}}{v_A^{3/2}} z$$

J_S and J_I are numerical constants of order unity obtained from simulation. ϵ is the cascade rate and v_F is the velocity at the forcing scale.

Chapter 2 ALFVÉN WAVES

2.1 Basic Equations

The equations which govern magnetohydrodynamics (MHD) are

$$\rho\left(\partial_t \mathbf{v} + \mathbf{v}\cdot\boldsymbol{\nabla}\mathbf{v}\right) = -\boldsymbol{\nabla}\left(p + \frac{B^2}{8\pi}\right) + \frac{1}{4\pi}\mathbf{B}\cdot\boldsymbol{\nabla}\mathbf{B} + \rho\nu_v\nabla^2\mathbf{v}, \tag{2.1}$$

$$\partial_t \mathbf{B} = \boldsymbol{\nabla}\times(\mathbf{v}\times\mathbf{B}) + \nu_B\nabla^2\mathbf{B}, \tag{2.2}$$

$$\partial_t \rho + \boldsymbol{\nabla}\cdot(\rho\mathbf{v}) = 0, \tag{2.3}$$

$$\boldsymbol{\nabla}\cdot\mathbf{B} = 0. \tag{2.4}$$

The concentration of a passive scalar advected by the fluid evolves according to

$$\partial_t c + \boldsymbol{\nabla}\cdot(c\mathbf{v}) = \nu_c\nabla^2 c \tag{2.5}$$

$\mathbf{v}$	fluid velocity	$\mathbf{B}$	magnetic field
ρ	fluid density	p	fluid pressure
c	passive scalar concentration	ν_v	momentum diffusivity
ν_B	magnetic diffusivity	ν_c	passive scalar diffusivity

We simplify equations (2.1)-(2.5) for applications in this paper.[1] Incompressibility is assumed throughout, so we set $\rho = 1$ and define the total pressure $P = p + B^2/8\pi$. The magnetic field is measured in velocity units by $\mathbf{b} \equiv \mathbf{B}/\sqrt{4\pi}$. Each diffusive term is replaced by a n'th order hyperdiffusivity with the same coefficient ν_n. With these modifications, equations (2.1)-(2.5) transform to

$$\partial_t \mathbf{v} = -\mathbf{v}\cdot\boldsymbol{\nabla}\mathbf{v} - \boldsymbol{\nabla}P + \mathbf{b}\cdot\boldsymbol{\nabla}\mathbf{b} + \nu_n\nabla^{2n}\mathbf{v}, \tag{2.6}$$

[1] Further steps are taken in §4.2 to cast these equations in a form suitable for computation.

$$\partial_t \mathbf{b} = -\mathbf{v} \cdot \boldsymbol{\nabla} \mathbf{b} + \mathbf{b} \cdot \boldsymbol{\nabla} \mathbf{v} + \nu_n \nabla^{2n} \mathbf{b}, \tag{2.7}$$

$$\boldsymbol{\nabla} \cdot \mathbf{v} = 0, \tag{2.8}$$

$$\boldsymbol{\nabla} \cdot \mathbf{b} = 0. \tag{2.9}$$

$$\partial_t c + \mathbf{v} \cdot \boldsymbol{\nabla} c = \nu_n \nabla^{2n} c. \tag{2.10}$$

To relate P to $\mathbf{v}$ and $\mathbf{b}$, we take the divergence of equation (2.6) which yields

$$\nabla^2 P = \boldsymbol{\nabla} \mathbf{b} : \boldsymbol{\nabla} \mathbf{b} - \boldsymbol{\nabla} \mathbf{v} : \boldsymbol{\nabla} \mathbf{v}. \tag{2.11}$$

Thus

$$P = \int \frac{d^3 x'}{4\pi} \frac{(\boldsymbol{\nabla} \mathbf{v} : \boldsymbol{\nabla} \mathbf{v} - \boldsymbol{\nabla} \mathbf{b} : \boldsymbol{\nabla} \mathbf{b})}{|\mathbf{x}' - \mathbf{x}|}. \tag{2.12}$$

2.2 Regimes

We decompose the magnetic field into a uniform part plus fluctuations;

$$\mathbf{b} = \langle \mathbf{b} \rangle + \Delta \mathbf{b}, \tag{2.13}$$

where $\langle \mathbf{b} \rangle = v_A \hat{\mathbf{z}}$ with v_A the Alfvén speed. Energies corresponding to these components are denoted by $E_{\langle \mathbf{b} \rangle}$, $E_{\mathbf{v}}$, and $E_{\Delta \mathbf{b}}$, respectively. The parameter

$$\mu = \frac{E_{\mathbf{v}} + E_{\Delta \mathbf{b}}}{E_{\langle \mathbf{b} \rangle}}, \tag{2.14}$$

which measures the relative importance of the fluctuations compared to the uniform field, determines the character of MHD turbulence.

MHD turbulence with small μ can be described in terms of interacting waves. Kinetic and potential energy are freely interchanged so $E_{\mathbf{v}}$ and $E_{\Delta \mathbf{b}}$ have comparable magnitudes. Wavemode turbulence is the principal subject of this thesis. Analytic scalings are presented in §3 to provide an intuitive feel for its dynamics. Results from our simulations are described in §5 and discussed in §6.

We offer a brief comment on MHD turbulence with large μ, although strictly speaking it is not part of this investigation. Suppose energy is input on outer scale L at a rate sufficient to maintain $\mu \gg 1$. Then the effect of the magnetic stress on large scale motions is negligible, and on these scales MHD turbulence resembles hydrodynamic turbulence. But the Kolmogorov scaling implies that the energy density in eddies of size $\lambda < L$ is of order $(\lambda/L)^{2/3}\mu$ times that in the mean magnetic field. Thus on scales below $\lambda \sim \mu^{3/2}L$, MHD turbulence with $\mu \gg 1$ is similar to that with $\mu \ll 1$.[2]

2.3 Linear Waves In Incompressible MHD

Linear perturbations about a uniform background magnetic field can be decomposed into shear Alfvén and pseudo Alfvén waves. The pseudo Alfvén wave is the incompressible limit of the slow magnetosonic wave.[3] As is well known, both waves conform to the dispersion relation

$$\omega^2 = v_A^2 k_z^2. \tag{2.15}$$

Eigenvectors for these modes take the form

$$\hat{\mathbf{v}}_A(\mathbf{k},t) = \hat{\mathbf{a}}(\mathbf{k}) \exp i\mathbf{k}\cdot(\mathbf{x} \mp v_A t\hat{\mathbf{z}}), \qquad \hat{\mathbf{b}}_A(\mathbf{k},t) = \mp\hat{\mathbf{a}}(\mathbf{k}) \exp i\mathbf{k}\cdot(\mathbf{x} \mp v_A t\hat{\mathbf{z}}), \tag{2.16}$$

$$\hat{\mathbf{v}}_S(\mathbf{k},t) = \hat{\mathbf{s}}(\mathbf{k}) \exp i\mathbf{k}\cdot(\mathbf{x} \mp v_A t\hat{\mathbf{z}}), \qquad \hat{\mathbf{b}}_S(\mathbf{k},t) = \mp\hat{\mathbf{s}}(\mathbf{k}) \exp i\mathbf{k}\cdot(\mathbf{x} \mp v_A t\hat{\mathbf{z}}), \tag{2.17}$$

where the unit polarization vectors are defined by

$$\hat{\mathbf{a}} \equiv \frac{\hat{\mathbf{k}} \times \hat{\mathbf{z}}}{[1 - (\hat{\mathbf{k}}\cdot\hat{\mathbf{z}})^2]^{1/2}}, \qquad \hat{\mathbf{s}} \equiv \frac{\hat{\mathbf{z}} - (\hat{\mathbf{k}}\cdot\hat{\mathbf{z}})\hat{\mathbf{k}}}{[1 - (\hat{\mathbf{k}}\cdot\hat{\mathbf{z}})^2]^{1/2}}. \tag{2.18}$$

We note that $\hat{\mathbf{k}}$, $\hat{\mathbf{s}}$, and $\hat{\mathbf{a}}$ form a right-hand triad.

MHD turbulence is anisotropic with power cascading more rapidly to high $k_\perp$ than

[2] Our discussion has ignored the amplification of magnetic energy by field line stretching due to eddies with $\lambda/L \gg \mu^{3/2}$ which would cause μ to decrease with time.

[3] In the limit of incompressibility the fast magnetosonic wave has infinite phase velocity and cannot be excited.

to high k_z. In the limit $k_\perp \gg k_z$, $\hat{\mathbf{s}} \to \hat{\mathbf{z}}$; displacements associated with slow modes align along the unperturbed magnetic field.

2.4 Elsasser Variables

The Elsasser transformation

$$\mathbf{w}_\uparrow = v_A\hat{\mathbf{z}} + \mathbf{v} - \mathbf{b} \qquad \mathbf{w}_\downarrow = -v_A\hat{\mathbf{z}} + \mathbf{v} + \mathbf{b} \tag{2.19}$$

applied to equations (2.6) and (2.7) with $\nu_n = 0$ brings out the two wave characteristics

$$\partial_t \mathbf{w}_\uparrow + v_A\partial_z \mathbf{w}_\uparrow = -\mathbf{w}_\downarrow \cdot \boldsymbol{\nabla}\mathbf{w}_\uparrow - \boldsymbol{\nabla}P, \tag{2.20}$$

$$\partial_t \mathbf{w}_\downarrow - v_A\partial_z \mathbf{w}_\downarrow = -\mathbf{w}_\uparrow \cdot \boldsymbol{\nabla}\mathbf{w}_\downarrow - \boldsymbol{\nabla}P, \tag{2.21}$$

where from equation (2.12),

$$P = \int \frac{d^3x'}{4\pi} \frac{\boldsymbol{\nabla}\mathbf{w}_\uparrow : \boldsymbol{\nabla}\mathbf{w}_\downarrow}{|\mathbf{x}' - \mathbf{x}|}. \tag{2.22}$$

Linear waves propagate at the Alfvén speed v_A either parallel ($\mathbf{w}_\uparrow$) or anti-parallel ($\mathbf{w}_\downarrow$) to the direction of the background magnetic field.

2.5 Collisions Between Wave Packets

Weak disturbances of the background field may be decomposed into upward ($\mathbf{w}_\uparrow$) and downward ($\mathbf{w}_\downarrow$) propagating wave packets. In the special case of unidirectional propagation either $\mathbf{w}_\uparrow = 0$ or $\mathbf{w}_\downarrow = 0$, and an arbitrary nonlinear wave packet is an exact solution of the equations of incompressible MHD (Parker 1979). To prove this, take the divergence of the equation for the nonzero $\mathbf{w}$. This yields $\nabla^2 P = 0$ which, since it applies globally, implies $\boldsymbol{\nabla}P = 0$, and hence that the wave packet propagates without distortion. An important corollary is that nonlinear distortions occur only

during collisions between oppositely directed wave packets.

Collisions are constrained by the conservation laws of energy,

$$E = \frac{1}{2}\int d^3x \left(|\mathbf{v}|^2 + |\mathbf{b}|^2\right), \tag{2.23}$$

and cross helicity,

$$I = \frac{1}{2}\int d^3x\, \mathbf{v}\cdot\mathbf{b}. \tag{2.24}$$

These conservation laws follow directly from equations (2.6)-(2.9) in the limit that $\nu_n = 0$. As a consequence, energy is not exchanged between colliding wave packets. A short proof follows.

Take the dot product of equations (2.20) and (2.21) with $\mathbf{w}_\uparrow$ and $\mathbf{w}_\downarrow$, respectively. The advective and pressure gradient terms reduce to total divergences. This establishes that

$$\frac{d}{dt}\int d^3x\, |\mathbf{w}_\uparrow|^2 = \frac{d}{dt}\int d^3x\, |\mathbf{w}_\downarrow|^2 = 0 \tag{2.25}$$

provided $\mathbf{w}_\uparrow$ and $\mathbf{w}_\downarrow$ either vanish at infinity or satisfy periodic boundary conditions. Now all that remains is to show that

$$E_\uparrow = \frac{1}{4}\int d^3x\, |\mathbf{w}_\uparrow|^2 \quad \text{and} \quad E_\downarrow = \frac{1}{4}\int d^3x\, |\mathbf{w}_\downarrow|^2 \tag{2.26}$$

are the energies of isolated upward and downward propagating wave packets. Clearly the total energy in the wave packets is

$$E = \frac{1}{2}\int d^3x \left(|\mathbf{v}|^2 + |\mathbf{b}|^2 - v_A^2\right). \tag{2.27}$$

Moreover, the definitions of the Elsasser variables lead to the identity

$$\int d^3x \left(|\mathbf{w}_\uparrow|^2 + |\mathbf{w}_\downarrow|^2\right) = 2\int d^3x \left(|\mathbf{v}|^2 + |\mathbf{b}|^2 + v_A^2 - 2v_A b_z\right). \tag{2.28}$$

Lastly, as is easily verified from the induction equation (2.9), flux conservation implies

$$\int d^3x \ (v_A - b_z) = 0. \tag{2.29}$$

Together, equations (2.27)-(2.29) demonstrate that $E_\uparrow$ and $E_\downarrow$ are the energies of isolated upward and downward propagating wave packets. Then equation (2.25) completes the proof that wave packet collisions are elastic.

2.6 Wave Packets Move Along Field Lines

To lowest nonlinear order in the wave amplitudes, distortions suffered in collisions between oppositely directed wave packets arise because each packet moves along field lines perturbed by the other. The proof follows directly from equation (2.20) written to second order in the amplitudes of the $\mathbf{w}_\uparrow$ and $\mathbf{w}_\downarrow$ fields. With the aid of equation (2.22), it can be shown that

$$D_\uparrow \left(\mathbf{w}_\uparrow^{(2)} + \boldsymbol{\xi}^{(1)} \cdot \boldsymbol{\nabla} \mathbf{w}_\uparrow^{(1)} + \boldsymbol{\nabla} \int \frac{d^3x'}{4\pi} \frac{\boldsymbol{\nabla}\boldsymbol{\xi}^{(1)} : \boldsymbol{\nabla}\mathbf{w}_\uparrow^{(1)}}{|\mathbf{x}' - \mathbf{x}|} \right) = 0. \tag{2.30}$$

Here

$$D_\uparrow \equiv \left(\frac{\partial}{\partial t} + v_A \frac{\partial}{\partial z} \right), \tag{2.31}$$

and

$$\mathbf{x}(\mathbf{x}_0, t) \equiv \mathbf{x}_0 + \boldsymbol{\xi}(\mathbf{x}_0, t). \tag{2.32}$$

The Lagrangian displacement, $\boldsymbol{\xi}$, connects the Lagrangian coordinate of a fluid particle, $\mathbf{x}_0$, to its Eulerian coordinate, $\mathbf{x}$.

Several steps are needed to establish equation (2.30). In terms of $\boldsymbol{\xi}$,

$$\mathbf{v} = \left. \frac{\partial \boldsymbol{\xi}}{\partial t} \right|_{\mathbf{x}_0}, \qquad \mathbf{b} = v_A \hat{\mathbf{z}} + v_A \left. \frac{\partial \boldsymbol{\xi}}{\partial z_0} \right|_t. \tag{2.33}$$

To first order in the amplitudes of $\mathbf{w}_\uparrow$ and $\mathbf{w}_\downarrow$, we may replace $\mathbf{x}_0$ by $\mathbf{x}$ in the definition

of $\boldsymbol{\xi}$ and write

$$\mathbf{v}^{(1)} = \frac{\partial \boldsymbol{\xi}^{(1)}}{\partial t}\bigg|_{\mathbf{x}}, \qquad \mathbf{b}^{(1)} = v_A \frac{\partial \boldsymbol{\xi}^{(1)}}{\partial z}\bigg|_{t}. \tag{2.34}$$

It then follows from equations (2.19) and (2.34) that

$$\mathbf{w}_{\downarrow}^{(1)} = D_{\uparrow}\boldsymbol{\xi}^{(1)}. \tag{2.35}$$

The final step is to verify that the linear operator $D_{\uparrow}$ passes through the integral sign and changes $\boldsymbol{\xi}^{(1)}$ to $\mathbf{w}_{\downarrow}^{(1)}$ while leaving the rest of the integrand unaltered.

Equation (2.30) has a simple interpretation. Consider an upward moving wave packet for which $\mathbf{w}_{\uparrow}^{(2)} = 0$ prior to its interaction with downward moving waves. Subsequent to this interaction suppose that $\boldsymbol{\xi}^{(1)}$ at fixed $z_{\uparrow} = z - v_A t$ is changed by $\Delta\boldsymbol{\xi}^{(1)}$. Then as a function of $z_{\uparrow}$

$$\Delta\mathbf{w}_{\uparrow}^{(2)} = -\Delta\boldsymbol{\xi}^{(1)} \cdot \boldsymbol{\nabla}\mathbf{w}_{\uparrow} - \boldsymbol{\nabla} \int \frac{d^3x'}{4\pi} \frac{\boldsymbol{\nabla}\Delta\boldsymbol{\xi}^{(1)} : \boldsymbol{\nabla}\mathbf{w}_{\uparrow}^{(1)}}{|\mathbf{x}' - \mathbf{x}|}. \tag{2.36}$$

The first term on the right-hand side of this equation is the perturbation that would result from the unconstrained displacement of $\mathbf{w}_{\uparrow}^{(1)}$ by $\Delta\boldsymbol{\xi}^{(1)}$. The second term constrains the perturbation to preserve $\boldsymbol{\nabla} \cdot \mathbf{w}_{\uparrow}^{(2)} = 0$.[4] Since magnetic field lines are frozen in the fluid, we conclude that, at least to second order, wave packets follow magnetic field lines. The turbulent energy cascade is associated with the shear of the $\Delta\boldsymbol{\xi}^{(1)}$ field. Uniform displacements, which arise as a consequence of the sweeping of small disturbances by larger ones, do not contribute to the transfer of energy across scales.

The proof in this section has been couched in Eulerian coordinates. A technically simpler version in Lagrangian coordinates is given by Sridhar and Goldreich (1994). It consists of demonstrating that the third order Lagrangian density for incompressible MHD vanishes when written in terms of the transverse components of the displacement vector. Although simpler technically, the Lagrangian based result is more subtle

[4]This term arises from the gradient of the total pressure.

conceptually. Its proper interpretation is provided in Goldreich & Sridhar(1997).[5]

[5]Henceforth we refer to Goldreich & Sridhar (1995) and (1997) separately as GSI and GSII, and together as GS.

Chapter 3 MHD CASCADES

A variety of models have been proposed for MHD turbulence. They share the common feature that energy cascades from lower to higher wave number.

3.1 The Irosnikov-Kraichnan Model

The standard model is that due to Irosnikov (1963) and Kraichnan (1965). Kraichnan's derivation of the IK spectrum relies on the fact that only oppositely directed waves interact in incompressible MHD. It assumes explicitly that the turbulence is isotropic and implicitly that the dominant interactions are those which couple three waves.

The above assumptions imply that the cascade time across scale λ is

$$t_c \sim \left(\frac{v_A}{v_\lambda}\right)^2 \frac{\lambda}{v_A}. \tag{3.1}$$

Setting v_λ^2/t_c equal to the dissipation rate per unit mass, ϵ, then yields

$$v_\lambda \sim (\epsilon v_A \lambda)^{1/4}, \tag{3.2}$$

which corresponds to the 1D power spectrum[1]

$$E(k) \sim \frac{(\epsilon v_A)^{1/2}}{k^{3/2}}. \tag{3.3}$$

Nonlinearity is measured by $\chi \sim (v_\lambda/v_A)$, where $N \sim \chi^{-2}$ is the number of wave periods in t_c;

$$\chi \sim \left(\frac{\epsilon\lambda}{v_A^3}\right)^{1/4}. \tag{3.4}$$

[1]Because the IK cascade is isotropic, it is sufficient to specify its 1D power spectrum.

Since χ decreases with decreasing λ, only dissipation limits the length of the IK inertial range.

The IK model is flawed because the assumption of isotropy is inconsistent with the frequency and wavevector closure relations that resonant triads must satisfy (Shebalin et al., 1983). These take the form

$$\omega_1 + \omega_2 = \omega_3, \tag{3.5}$$

$$\mathbf{k}_1 + \mathbf{k}_2 = \mathbf{k}_3. \tag{3.6}$$

But since $\omega = v_A|k_z|$, equation (3.5) and the z component of equation (3.6) yield the set

$$|k_{1z}| + |k_{2z}| = |k_{3z}| \tag{3.7}$$

$$k_{1z} + k_{2z} = k_{3z}. \tag{3.8}$$

Because nonlinear interactions can only occur between oppositely directed waves, the 3-mode coupling coefficient vanishes unless waves 1 and 2 propagate in opposite directions. In that case, equations (3.7) and (3.8) imply that either k_{1z} or k_{2z} must vanish. Since one of the incoming waves has zero frequency, 3-wave interactions do not cascade energy along k_z.

3.2 Intermediate MHD Turbulence

GSII propose an anisotropic MHD cascade based on scalings obtained from 3-wave interactions. It represents a new form of turbulence, which they term intermediate, because it shares some of the properties of both weak and strong turbulence. Although individual wave packets suffer small distortions in single collisions, interactions of all orders make comparable contributions to the perpendicular cascade.[2]

To derive the scaling relations for the intermediate cascade, we repeat the steps

[2]This is a controversial claim.

carried out in §3.1 for the IK model, but with $\lambda_\perp$ in place of λ and $\lambda_\parallel$ held constant. Here $\lambda_\perp$ and $\lambda_\parallel$ are correlation lengths in directions perpendicular and parallel to the local magnetic field. Thus

$$t_c \sim \left(\frac{v_A \lambda_\perp}{v_{\lambda_\perp} \lambda_\parallel}\right)^2 \frac{\lambda_\parallel}{v_A}. \tag{3.9}$$

Setting $\epsilon \sim v_{\lambda_\perp}^2 / t_c$, we find

$$v_{\lambda_\perp} \sim \left(\frac{\epsilon v_A \lambda_\perp^2}{\lambda_\parallel}\right)^{1/4}, \tag{3.10}$$

and

$$E(k_\perp) \sim \frac{\left(\epsilon v_A k_\parallel\right)^{1/2}}{k_\perp^2}. \tag{3.11}$$

Besides being anisotropic, the intermediate MHD cascade differs from the IK cascade in another important respect. The strength of nonlinear interactions, as measured by

$$\chi \sim \left(\frac{v_{\lambda_\perp} \lambda_\parallel}{v_A \lambda_\perp}\right) \sim \left(\frac{\epsilon \lambda_\parallel^3}{v_A^3 \lambda_\perp^2}\right)^{1/4}, \tag{3.12}$$

increases along the cascade. Thus, even in the absence of dissipation, the intermediate cascade has a finite inertial range. This suggests that a strong form of MHD turbulence must be the relevant one for most applications in nature.

3.3 Strong MHD Turbulence

A cascade for strong MHD turbulence is described in GSI. Its defining property is that MHD waves suffer order unity distortions on time scales comparable to their periods. GSI argue that the quantity χ defined in equation (3.12) saturates at a value of order unity. This state is referred to as one of critical balance. Together with the assumption of a constant energy flux along the cascade, as expressed by

$$\epsilon \sim \frac{v_{\lambda_\perp}^3}{\lambda_\perp}, \tag{3.13}$$

it implies that

$$\lambda_\parallel \propto \lambda_\perp^{2/3}. \tag{3.14}$$

Although there is a parallel cascade of energy in strong MHD turbulence, the degree of anisotropy increases along the cascade.

Let us assume $v_L \sim v_A$ and isotropy on scale outer scale L. Then the 3D energy spectrum of strong MHD turbulence takes the form

$$E(k_\perp, k_\parallel) \sim \frac{v_A^2}{L^{1/3} k_\perp^{10/3}} f\left(\frac{k_\parallel L^{1/3}}{k_\perp^{2/3}}\right), \tag{3.15}$$

where $f(u)$ is a positive symmetric function of u with the properties that $f(u) \approx 1$ for $|u| \lesssim 1$ and $f(u)$ negligibly small for $|u| \gg 1$. The power spectrum is flat as a function of $k_\parallel$ for $k_\parallel \lesssim k_\perp^{2/3} L^{-1/3}$ because the velocity and magnetic perturbations on transverse scale $k_\perp^{-1}$ arise from independent wave packets whose lengths $\lambda_\parallel \sim \lambda_\perp^{2/3} L^{1/3}$. The 1D perpendicular power spectrum obtained from equation (3.15) reads

$$E(k_\perp) \sim \frac{v_A^2}{L^{2/3} k_\perp^{5/3}}. \tag{3.16}$$

Thus the spectrum of strong MHD turbulence is an anisotropic version of the Kolmogorov (1941) spectrum for hydrodynamic turbulence.

Inertial range velocity differences and magnetic perturbations across perpendicular scale $\lambda_\perp$ satisfy

$$v_{\lambda_\perp} \sim b_{\lambda_\perp} \sim \left(\frac{\lambda_\perp}{L}\right)^{1/3} v_A. \tag{3.17}$$

Thus even though the turbulence is properly classified as strong, deep in the inertial range magnetic field lines are nearly parallel across perpendicular separations $\lambda_\perp$ and nearly straight along parallel separations $\lambda_\parallel$; differential bending angles are of order $(\lambda_\perp/L)^{1/3} \sim (\lambda_\parallel/L)^{1/2}$.

3.3.1 Parallel Cascade

It is interesting to examine the frequency changing interactions that drive the parallel cascade. Referring back to the intermediate cascade, we know that 3-wave interactions do not change frequencies. However, interactions involving more than 3-waves can.

For example, frequency changes arise in 4-wave interactions of the form

$$\omega_1 + \omega_2 + \omega_3 = \omega_4, \tag{3.18}$$

$$\mathbf{k}_1 + \mathbf{k}_2 + \mathbf{k}_3 = \mathbf{k}_4, \tag{3.19}$$

where k_{1z} and k_{2z} have the same sign and $\omega_3 = v_A|k_{3z}| = 0$ (Ng & Bhattacharjee, 1996; GKII). The parallel cascade they give rise to proceeds at a rate which is smaller than that of the perpendicular cascade by a factor of order χ. Because strong MHD turbulence is characterized by $\chi \sim 1$, it has a significant parallel cascade.

3.3.2 Field Line Geometry

MHD turbulence is best understood geometrically. Field lines perturbed by waves propagating in one direction define two-dimensional mappings between xy planes separated by distance z. Shear Alfvén waves dominate the shear and slow waves the dilatation of these mappings. The magnitude of the shear exceeds that of the dilatation by a factor of order $\lambda_{\parallel}/\lambda_{\perp} \sim (L/\lambda_{\perp})^{1/3} \gg 1$. These mappings describe the distortion that counter propagating waves would suffer if they moved at uniform speed along the perturbed field lines. The dominance of the shear over the dilatation explains why shear Alfvén waves control the perpendicular cascades of both types of wave.

The recognition that MHD waves tend to follow field lines is essential to understanding their turbulent cascades. Figure 3.1 provides a visual illustration of how this works. The left-hand panel displays a snapshot of field lines perturbed by downward propagating waves. In the right-hand panel we follow the evolution of a horizontal pattern as it propagates from the bottom to the top following these lines. The distortion of the initially circular bullseye is principally due to the shear in the two-dimensional mapping defined by the perturbed field lines. The cascade time on the scale of the initial pattern is that over which the shear grows to order unity.

This geometrical picture requires two qualifications. The first is that the propagation speed of MHD waves is not exactly constant but varies with the strength of the

local magnetic field. Pressure perturbations associated with slow waves are balanced by perturbations of magnetic pressure. The resulting perturbations in propagation speed, of order $v_{\lambda_\perp}$, contribute to the nonlinear cascade. Over one wave period they lead to fractional distortions of order $v_{\lambda_\perp}/v_A \sim \lambda_\perp/\lambda_\parallel \ll 1$. Thus they are properly ignored. The second qualification is that MHD waves do not exactly follow field lines. The extent to which this effects their cascade remains to be quantified.

The parallel cascade may also be viewed in geometrical terms. Consider an upward propagating wave packet of length $\lambda_\parallel$ and width $\lambda_\perp$ which is being distorted by downward moving wave packets of similar scale. Correlations along the parallel direction are shortened because the front and back of the wave packet undergo different 2-dimensional mappings. This happens because the upward propagating packet distorts each downward going packet as it passes through it. This distortion is of order χ. For strong MHD turbulence $\chi \sim 1$ which accounts for its significant parallel cascade.

Incidentally, the geometrical picture also aids the interpretation of results from perturbation theory. For example, the 3-wave resonant interactions which dominate the perpendicular cascade and the 4-wave resonant interactions which cause the lowest order frequency changes each depend upon the amplitudes of modes with $k_z = 0$. This is because the shear in the mapping between xy planes separated by Δz is proportional to the displacement amplitudes of modes with $k_z \lesssim 1/\Delta z$. Perturbation theory corresponds to the limit of vanishing cascade strength in which shears of order unity are achieved in the limit of infinite separation along the z-axis.

3.3.3 Relation to 2D Hydrodynamic Turbulence

Magnetic field lines possess a tension which makes them ill-disposed to bend, but they are easily shuffled. This accounts for the 2D character of MHD turbulence. It also prompts an inquiry about the relation of MHD turbulence to 2D hydrodynamic turbulence. Each fluid element conserves its vorticity in inviscid 2D hydrodynamics. This results in a direct cascade of enstrophy (vorticity squared) toward high $k_\perp$ and

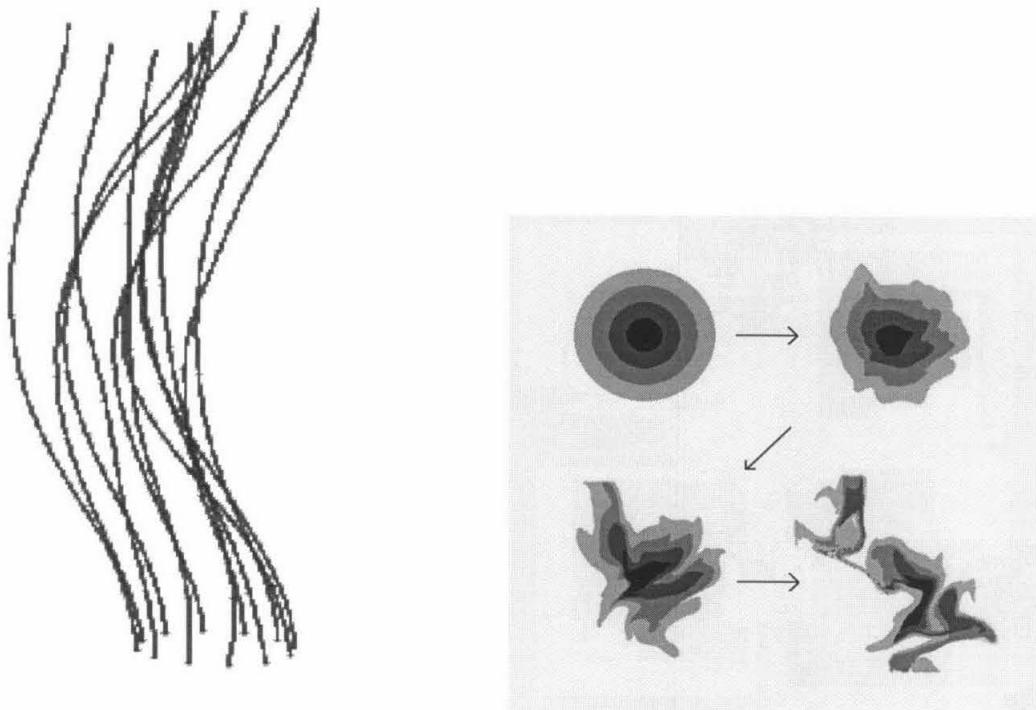

Figure 3.1: *Wavepacket Distortion Through Fieldline Wander.*

The left-hand panel displays a sample of field lines perturbed by downward propagating waves. The distortion of an originally circular bullseye pattern as it moves upward following these field lines is shown in the right-hand panel.

an inverse cascade of energy toward small $k_\perp$ (Lesieur 1990). As we now demonstrate, MHD turbulence does not share these characteristics.

The vorticity equation in MHD, obtained by taking the curl of equation (2.6) with $\nu_n = 0$, reads

$$\frac{\partial(\boldsymbol{\nabla} \times \mathbf{v})}{\partial t} = \boldsymbol{\nabla} \times [\mathbf{v} \times (\boldsymbol{\nabla} \times \mathbf{v}) - \mathbf{b} \times (\boldsymbol{\nabla} \times \mathbf{b})]\,. \tag{3.20}$$

We concentrate on shear Alfvén waves since they dominate the field aligned vorticity for nearly perpendicular cascades. Scaling the terms in equation (3.20) shows that

$$\frac{\partial \omega_\parallel}{\partial t} \sim \frac{v_{\lambda_\perp}}{\lambda_\perp} \omega_\parallel. \tag{3.21}$$

Thus $\omega_\parallel$ changes on the cascade time scale; it is not even approximately conserved. Consequently, there is no enstrophy constraint to prevent energy from cascading toward larger $k_\perp$.

Chapter 4 SIMULATION STRATEGY

What follows is a comprehensive discussion of the techniques used in our simulations. We begin by introducing the notation we adopt.

4.1 Spectral Notation

Cartesian coordinates are distinguished by Greek indices which run from $1-3$. Simulations are carried out in boxes whose sides have lengths L_α and corresponding grid sizes N_α. Integer coordinate components, l_α, and integer wavevector components, s_α, are defined through the relations

$$x_\alpha = \frac{L_\alpha}{N_\alpha} l_\alpha, \text{ where } 0 \leq l_\alpha < N_\alpha, \tag{4.1}$$

and

$$k_\alpha = \frac{2\pi}{L_\alpha} s_\alpha, \text{ where } -\frac{N_\alpha}{2} \leq s_\alpha \leq \frac{N_\alpha}{2}. \tag{4.2}$$

The discrete Fourier transform in 1D is given by

$$\tilde{q}(s) = \frac{1}{N} \sum_l q(l) e^{2\pi i s l/N}, \tag{4.3}$$

where the tilde, $\tilde{}$, denotes Fourier transform. Generalization to 3D is trivial.

4.2 Spectral Algorithm

4.2.1 Fourier Space Equations

We evolve the incompressible MHD equations in Fourier space where they take the form (Lesieur 1990)

$$\partial_t \tilde{v}_\alpha = -ik_\gamma \left(\delta_{\alpha\beta} - \tfrac{k_\alpha k_\beta}{k^2}\right)\left(\widetilde{v_\beta v}_\gamma - \widetilde{b_\beta b}_\gamma\right) - \nu_n k^{2n}\tilde{v}_\alpha \quad , \tag{4.4}$$

$$\partial_t \tilde{b}_\alpha = -ik_\beta(\widetilde{v_\beta b}_\alpha - \widetilde{b_\beta v}_\alpha) - \nu_n k^{2n}\tilde{b}_\alpha, \tag{4.5}$$

$$k_\alpha \tilde{v}_\alpha = 0, \tag{4.6}$$

$$k_\alpha \tilde{b}_\alpha = 0, \tag{4.7}$$

$$\partial_t \tilde{c} = -ik_\beta \widetilde{v_\beta c} - \nu_n k^{2n}\tilde{c}. \tag{4.8}$$

4.2.2 Integration Method

Equations (4.4), (4.5), and (4.8) constitute a system of ordinary differential equations with time as the dependent variable and the Fourier coefficients $\{\tilde{v}_\alpha, \tilde{b}_\alpha, \tilde{c}\}$ as the independent variables. We employ a modified version of the second order Runge-Kutta algorithm (RK2) to advance the variables in time. First order algorithms are substantially less stable than RK2 at the same timestep.

RK2 advances the variables across an interval Δt in two stages. Derivatives evaluated at the initial time are used to compute trial values of the variables at the midpoint $\Delta t/2$. Then derivatives computed at $\Delta t/2$ with these trial values are used to advance the variables from $t = 0$ to Δt. In symbolic form

$$\tilde{q}_{\mathsf{trial}}(\Delta t/2) = \tilde{q}(0) + \partial_t \tilde{q}(0)\Delta t/2 \tag{4.9}$$

is followed by

$$\tilde{q}(\Delta t) = \tilde{q}(0) + \partial_t \tilde{q}(\Delta t/2)\Delta t, \tag{4.10}$$

where $\partial_t \tilde{q}(\Delta t/2)\Delta t$ is evaluated using $\tilde{q}_{\mathsf{trial}}(\Delta t/2)$. Each stage involves a first order Euler (E1) step in which the derivative is taken to be constant.

We make one departure from standard RK2 and treat diffusive terms with an integrating factor. Consider an equation of the form

$$\partial_t \tilde{q}(k) = A - \nu_n k^{2n} \tilde{q}(k), \tag{4.11}$$

where A comprises the non-diffusive terms. Its solution, with A constant throughout the interval Δt, is

$$\tilde{q}(\Delta t) = \left[\tilde{q}(0) + \frac{A}{\nu_n k^{2n}}(e^{\nu_n k^{2n}\Delta t} - 1)\right] e^{-\nu_n k^{2n}\Delta t} \tag{4.12}$$

We use this expression in place of E1 in each stage of RK2. To lowest order in $\nu_n k^{2n}\Delta t$, equation (4.12) reduces to E1. However, it has the advantage that it yields stable solutions to equation (4.11) with constant A for arbitrary values of $\nu_n k^{2n}\Delta t$ whereas E1 yields unstable solutions for $\nu_n k^{2n}\Delta t > 2$.

4.2.3 Dealiasing

Bilinear terms in equations (4.4), (4.5), and (4.8) are calculated by transforming the individual fields to real space, carrying out the appropriate multiplications there, and then transforming the products back to Fourier space. This requires $N_1 N_2 N_3$ operations using the Fast Fourier Transform (FFT) algorithm; $(N_1 N_2 N_3)^2$ operations would be needed to carry out the equivalent convolution in Fourier space.

This economy comes at the price of either a 1/3 reduction in resolution or an aliasing error (Canuto 1988). To appreciate this, consider the 1D product

$$\begin{aligned} \widetilde{pq}(s) &= \tfrac{1}{N}\textstyle\sum_l \left[\sum_{s'} \tilde{p}(s') e^{-2\pi i s' l/N} \sum_{s''} \tilde{q}(s'') e^{-2\pi i s'' l/N}\right] e^{2\pi i s l/N} \\ &= \tfrac{1}{N}\textstyle\sum_{s'}\sum_{s''} \tilde{p}(\mathbf{s}')\tilde{q}(s'') e^{2\pi i (s'+s'')l/N} \delta_{s,s'+s''+mN}, \end{aligned} \tag{4.13}$$

where m is any integer. The $m = 0$ terms comprise the convolution, and the remainder the aliasing error. To avoid the aliasing error, we set all Fourier components with $|s| > N/3$ to zero both before we compute the real space fields and again after we return

the bilinear terms to Fourier space. Truncation ensures that Fourier components of bilinear terms with $m \neq 0$ vanish. Its cost is the reduction of the effective spatial resolution from N to $2N/3$.

4.3 Spectral Wave Mode Decomposition

Separation of $\tilde{\mathbf{v}}(\mathbf{k})$ and $\tilde{\mathbf{b}}(\mathbf{k})$ into upward and downward propagating components is accomplished by forming Fourier coefficients of the Elsasser variables $\tilde{\mathbf{w}}_{\uparrow}(\mathbf{k})$ and $\tilde{\mathbf{w}}_{\downarrow}(\mathbf{k})$ according to

$$\tilde{\mathbf{w}}_{\uparrow}(\mathbf{k}) = \tilde{\mathbf{v}}(\mathbf{k}) - \tilde{\mathbf{b}}(\mathbf{k}) \qquad \tilde{\mathbf{w}}_{\downarrow}(\mathbf{k}) = \tilde{\mathbf{v}}(\mathbf{k}) + \tilde{\mathbf{b}}(\mathbf{k}). \tag{4.14}$$

Projections of $\tilde{\mathbf{w}}_{\uparrow}(\mathbf{k})$ and $\tilde{\mathbf{w}}_{\downarrow}(\mathbf{k})$ along the polarization directions of the linear incompressible MHD eigenmodes given by equation (2.18) yield amplitudes of upward and downward propagating Alfvén and slow waves. In obvious notation

$$A_{\uparrow}(\mathbf{k}) \equiv \hat{\mathbf{a}} \cdot \tilde{\mathbf{w}}_{\uparrow}(\mathbf{k}) = \tilde{v}_A(\mathbf{k}) - \tilde{b}_A(\mathbf{k}) \qquad S_{\uparrow}(\mathbf{k}) \equiv \hat{\mathbf{s}} \cdot \tilde{\mathbf{w}}_{\uparrow}(\mathbf{k}) = \tilde{v}_S(\mathbf{k}) - \tilde{b}_S(\mathbf{k}) \tag{4.15}$$

$$A_{\downarrow}(\mathbf{k}) \equiv \hat{\mathbf{a}} \cdot \tilde{\mathbf{w}}_{\downarrow}(\mathbf{k}) = \tilde{v}_A(\mathbf{k}) + \tilde{b}_A(\mathbf{k}) \qquad S_{\downarrow}(\mathbf{k}) \equiv \hat{\mathbf{s}} \cdot \tilde{\mathbf{w}}_{\downarrow}(\mathbf{k}) = \tilde{v}_S(\mathbf{k}) + \tilde{b}_S(\mathbf{k}) \tag{4.16}$$

where

$$\tilde{v}_A(\mathbf{k}) = \hat{\mathbf{a}} \cdot \tilde{\mathbf{v}}(\mathbf{k}) \qquad \tilde{b}_A(\mathbf{k}) = \hat{\mathbf{a}} \cdot \tilde{\mathbf{b}}(\mathbf{k}) \qquad \tilde{v}_S(\mathbf{k}) = \hat{\mathbf{s}} \cdot \tilde{\mathbf{v}}(\mathbf{k}) \qquad \tilde{b}_S(\mathbf{k}) = \hat{\mathbf{s}} \cdot \tilde{\mathbf{b}}(\mathbf{k}). \tag{4.17}$$

The eigenmode frame, $(\hat{\mathbf{k}}, \hat{\mathbf{s}}, \hat{\mathbf{a}})$, is tied to the direction of the mean field, $\hat{\mathbf{b}}_0 = \hat{\mathbf{z}}$, to which the local field direction, $\hat{\mathbf{b}}$, is inclined by an angle $\theta \sim v_{L_\perp}/v_A$. Consequently, our method for spectral decomposition erroneously mixes Alfvén and slow modes. However, for nearly transverse cascades the mixing is only of order $\theta^2 \ll 1$.

Field line tilt also causes k_r and k_z to differ from $k_\perp$ and $k_{||}$;

$$k_r = \cos\theta k_\perp + \sin\theta k_{||} \qquad k_z = -\sin\theta k_\perp + \cos\theta k_{||}. \tag{4.18}$$

Thus $k_r \approx k_\perp[1 + O(\theta^2)]$. However, $k_z \approx k_{||} + \theta k_\perp \approx \theta k_\perp$, where the final relation applies because the degree of anisotropy increases with increasing $k_\perp$ along MHD cascades. Thus, $k_\perp$ can be represented to acceptable accuracy by k_r. However, $k_{||}$ cannot be obtained from k_z. Henceforth, we treat as equivalent k_r and $k_\perp$ and $L_x = L_y$ and $L_\perp$. However, we are always careful to distinguish k_z from $k_{||}$ and to note that

$$k_z \approx \frac{v_{L_\perp}}{v_A} k_\perp. \tag{4.19}$$

4.4 Power Spectra

Three-dimensional power spectra of field quantities, $E_{3D}(\mathbf{k})$, are azimuthally symmetric functions of $\mathbf{k}_r = k_x\hat{\mathbf{x}} + k_y\hat{\mathbf{y}}$ at fixed k_z.[1] Accordingly, we define the 2D integrated power spectrum by

$$E_{2D}(k_r,\, k_z) = k_r \int_0^{2\pi} d\phi E_{3D}(\mathbf{k}). \tag{4.20}$$

It is important to note that $E_{2D}(k_r,\, k_z)$ is not equivalent to $E_{2D}(k_\perp,\, k_{||})$. Moreover, the latter cannot be derived from the former. This shortcoming is due to the failure of the spectral decomposition procedure described in §4.3 to determine $k_{||}$. It means that the 2D power spectrum is not a useful quantity.[2] However, we make so much use of the 1D integrated power spectrum defined by

$$E_{1D}(k_r) = \int_{-\infty}^{\infty} dk_z E_{2D}(k_r,\, k_z), \tag{4.21}$$

that henceforth we drop the subscript 1D.

4.5 Structure Functions

The 3D behavior of MHD turbulence is best captured in real space using second order structure functions tied to the local magnetic field. We define transverse and

[1] In any specific realization this is true only in a statistical sense.
[2] We obtain 2D information from structure functions.

longitudinal structure functions for the vector field $\mathbf{U}$ by

$$SFT_U(x_\perp) \equiv < [\mathbf{U}(\mathbf{x}' + \mathbf{x}_\perp) - \mathbf{U}(\mathbf{x}')] \cdot [\mathbf{U}(\mathbf{x}' + \mathbf{x}_\perp) - \mathbf{U}(\mathbf{x}')] >, \tag{4.22}$$

where $\mathbf{x}_\perp \cdot \mathbf{b} = 0$, and

$$SFL_U(x_\parallel) \equiv < [\mathbf{U}(\mathbf{x}' + \mathbf{f}(x_\parallel)) - \mathbf{U}(\mathbf{x}')] \cdot [\mathbf{U}(\mathbf{x}' + \mathbf{f}(x_\parallel)) - \mathbf{U}(\mathbf{x}')] >, \tag{4.23}$$

where $\mathbf{f}(x_\parallel) = \int_0^{x_\parallel} ds\, \hat{\mathbf{b}}(s)$. Averaging over $\mathbf{x}'$ is done with random volume sampling. Since the vector fields of interest possess statistical axial symmetry about $\hat{\mathbf{b}}$, we include an axial averaging of the direction of $\mathbf{x}_\perp$ at fixed $x_\perp \equiv |\mathbf{x}_\perp|$ in the computation of $SFT_U(x_\perp)$. The integral in the definition for $\mathbf{f}(x_\parallel)$ is taken along the field direction starting at $\mathbf{x}'$.

4.6 Timestep And Hyperviscosity

The anisotropy of MHD turbulence complicates the discussion of constraints on the timestep and hyperviscosity. Accordingly, we begin by discussing the simpler case of spectral simulation of isotropic hydrodynamic turbulence.

4.6.1 Isotropic Hydrodynamic Turbulence

We assume the Kolmogorov scaling. Given velocity v_L on outer scale L, inertial range velocity differences across $\lambda \lesssim L$ scale as $v_\lambda \sim (\lambda/L)^{1/3} v_L$ down to inner scale $\ell \sim (\nu_n / v_L L^{2n-1})^{3/(6n-2)} L$.

Four conditions constrain the values of the timestep, Δt, and hyperviscosity, ν_n, suitable for a spectral simulation of isotropic hydrodynamic turbulence. Each refers to the behavior of modes with the largest wavevectors, k_M. We express these constraints in terms of the dimensionless variables $\overline{\Delta t} \equiv v_L k_M \Delta t$ and $\overline{\nu} \equiv (\nu_n k_M^{2n})/(v_L k_M)$.

- Conditions 1) and 2) are concerned with computational accuracy.

1. Advection by outer scale eddies gives rise to fractional changes of order $v_L k_M \Delta t$ in the Fourier components of the smallest scale modes during one timestep.[3] Accurate computation requires

$$\overline{\Delta t} \lesssim 1, \tag{4.24}$$

which is the spectral equivalent of the Courant condition in real space.

2. Hyperviscosity causes a fractional decay of order $\nu_n k_M^{2n} \Delta t$ in the amplitudes of the smallest scale modes during a single timestep. Thus

$$\overline{\Delta t} \lesssim \frac{1}{\overline{\nu}_n}. \tag{4.25}$$

- Conditions 3) and 4) are required to maintain stability.

3. This constraint depends upon the algorithm used to advance the variables in time. Integration with RK2 results in an unphysical transfer of energy from large to small scale modes. Consider 1D uniform advection at speed v_L of the single Fourier mode $v(k_M, t)$. RK2 yields $v(k_M, \Delta t) = [1 - iv_L k_M \Delta t - (v_L k_M \Delta t)^2/2] v(k_M, 0)$. Thus $|v(k_M, \Delta t)|^2 = [1 + (v_L k_M \Delta t)^4/4] |v(k_M, 0)|^2$. In order that hyperviscosity maintain stability,

$$\overline{\Delta t} \lesssim (4\overline{\nu}_n)^{1/3}. \tag{4.26}$$

4. A turbulent cascade transfers energy from large to small scales where it is dissipated by viscosity. Spectral simulations of turbulence must include a mechanism which is able to dispose of the energy carried by the cascade before it reaches k_M. Otherwise it would reflect back to smaller k and the high k Fourier modes would approach energy equipartition with those of lower k.[4] Hyperviscosity suffices provided the inner scale it sets is larger

[3] Changes caused by interactions which are local in Fourier space are smaller by a factor $(k_M L)^{-1/3}$.

[4] The energy per Fourier mode scales as $k^{-11/3}$ in Kolmogorov turbulence.

than the grid resolution. This requires

$$\overline{\nu}_n \gtrsim (k_M L)^{-1/3} = (\pi N/2)^{-1/3}. \tag{4.27}$$

Dealiasing also involves a loss of energy and can stabilize simulations run with a sufficiently small timestep even in the absence of hyperviscosity. Further investigation is needed to clarify the manner in which energy is lost due to dealiasing.

4.6.2 Anisotropic Magnetohydrodynamic Turbulence

We restrict our discussion of MHD turbulence to cases in which the energy in the mean magnetic field greatly exceeds that in the kinetic and magnetic fluctuations. As discussed in Chapter 3, analytic arguments indicate that the Kolmogorov scaling is obeyed in planes perpendicular to the mean magnetic field. Thus constraints on the timestep and hyperviscosity deduced in §4.6.1 for hydrodynamic turbulence pertain to MHD turbulence in the xy plane provided we take $\overline{\Delta t} \equiv v_{L_\perp} k_{M_\perp} \Delta t$ and $\overline{\nu} \equiv (\nu_n k_{M_\perp}^{2n})/(v_{L_\perp} k_{M_\perp})$.

Different constraints arise from motion along the direction of the mean magnetic field. Strong MHD turbulence is anisotropic with energy cascading more rapidly along $k_\perp$ than along $k_\parallel$. Analytic arguments imply that the anisotropy at perpendicular scale $k_\perp^{-1}$ is determined by the condition that the nonlinearity parameter $\chi = (v_\lambda k_\perp)/(v_A k_\parallel) \sim 1$, where $k_\parallel$ is the wavevector component in the direction of the local magnetic field. It is important to maintain the distinction between $k_\parallel$ and k_z. As discussed in §4.3, $k_z \approx (v_{L_\perp}/v_A) k_\perp \sim (k_\perp L_\perp)^{1/3} k_\parallel$.

We control the value of $(v_{L_\perp} L_z)/(v_A L_\perp)$ in our simulations. Typically this quantity is set somewhat larger than unity in order to ensure that the largest scale structures cascade on a time scale shorter than the Alfvén crossing time L_z/v_A. As a consequence,

$$v_A k_{M_z} \approx \frac{v_A L_\perp}{v_{L_\perp} L_z} v_{L_\perp} k_{M_\perp} \lesssim v_{L_\perp} k_{M_\perp}. \tag{4.28}$$

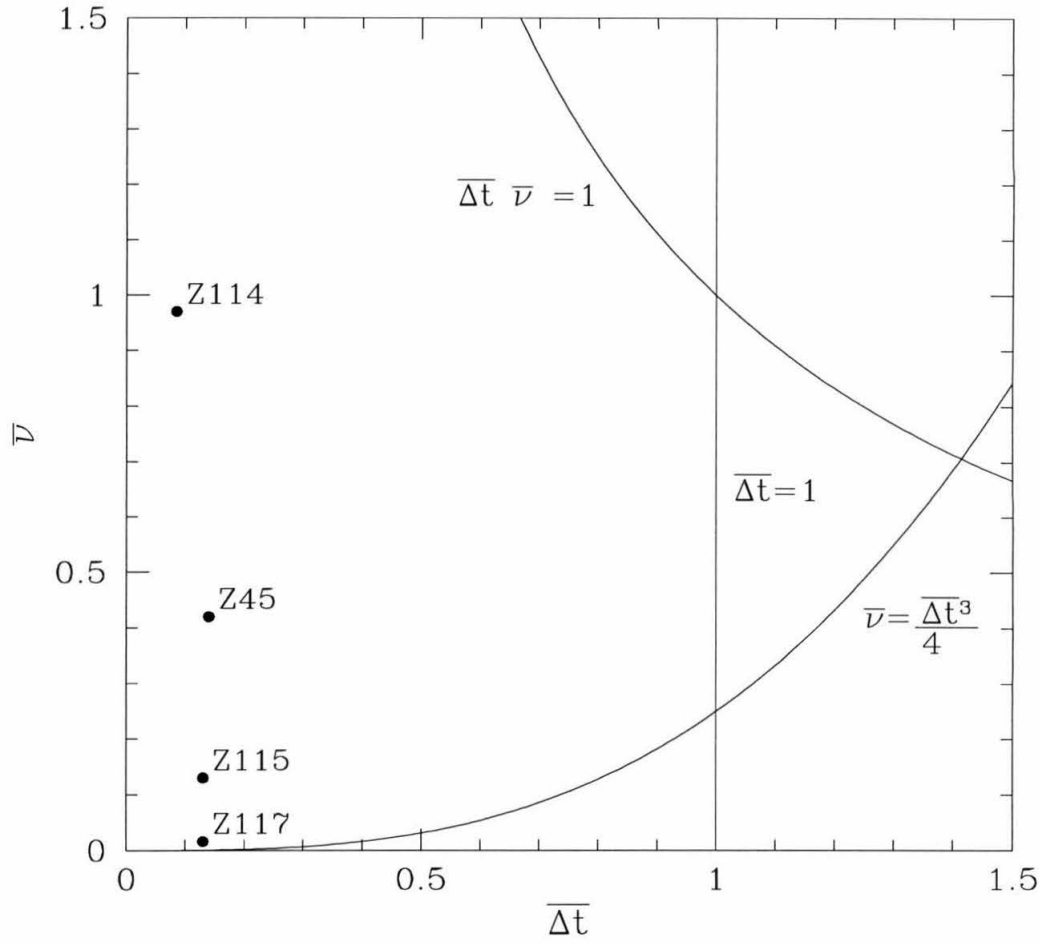

Figure 4.1: *Timestep and Hyperviscosity.*

We illustrate constraints on the dimensionless timestep and hyperviscosity as described in §4.6. The constraint given by equation (4.27) is not shown because it depends upon an additional parameter. Allowed choices lie in the simply connected region bounded by the upper left hand corner of the figure. Each plotted point represents values used in an individual simulation.

After this preparation, we are ready to examine the constraints placed on Δt and ν_n by evolution in the z direction.

1. Advection in the z direction is dominated by propagation at the Alfvén speed since $v_{L_z} \ll v_A$ in our simulations. Thus computational accuracy demands $v_A k_{M_z} \Delta t \lesssim 1$. Since $v_A k_{M_z} \lesssim v_{L_\perp} k_{M_\perp}$, this constraint is less severe than that imposed by equation (4.24).

2. Hyperdiffusivity is not important in the z direction because $k_{M_z} \ll k_{M_\perp}$ and we use a scalar hyperdiffusivity.

3. Integration with RK2 leads to an unphysical transfer of energy from large to small scales due to advection at the Alfvén speed. Provided equation (4.26) is satisfied, this does not cause any difficulty because $v_A k_{M_z} \lesssim v_{L_\perp} k_{M_\perp}$.

4. The maximum wave number in the z direction, k_{M_z}, must be larger than that at the inner scale of the cascade. From equation (4.19)

$$k_{M_z} L_z \sim \left(\frac{v_{L_\perp} L_z}{v_A L_\perp} \right) k_{M_\perp} L_\perp. \tag{4.29}$$

As mentioned above, the factor preceding $k_{M_\perp} L_\perp$ is typically larger than unity. Thus adequate resolution along z generally requires $N_z > N_\perp$.

4.7 Tests Of The Spectral Code

Time derivatives of field quantities computed with the spectral code agree with those obtained from a finite difference program with an elliptic incompressible pressure operator. Although the latter is unstable, it offers an independent method for computing time derivatives.

The code preserves the solinoidal character of $\mathbf{v}$ and $\mathbf{b}$. To machine accuracy it returns $\mathbf{k} \cdot \partial_t \tilde{\mathbf{v}}(\mathbf{k}) = 0$ and $\mathbf{k} \cdot \partial_t \tilde{\mathbf{b}}(\mathbf{k}) = 0$. It also conserves energy. Provided $\nu_n = 0$, it yields $\partial_t E = \sum_{\mathbf{k}} \tilde{\mathbf{v}}(\mathbf{k}) \cdot \partial_t \tilde{\mathbf{v}}(\mathbf{k}) + \tilde{\mathbf{b}}(\mathbf{k}) \cdot \partial_t \tilde{\mathbf{b}}(\mathbf{k}) = 0$, again to machine accuracy.

Harmonic Alfvén waves are evolved by our spectral code in a manner consistent with their analytic dispersion relation.

Results obtained from a simulation of decaying hydrodynamic turbulence (Z45) run with our code agree with those from a more thorough simulation by Jimenez et al. (1993). Our simulation is carried out in a cubic box with $L = 1.0$, has resolution 256^3, kinematic viscosity $\nu = 8 \cdot 10^{-4}$, timestep $\Delta t = 2.5 \times 10^{-4}$, and is initialized with rms velocity $v = 1.0$. We compute components of the velocity gradient longitudinal, $\nabla_{||} v_{||}$, and transverse, $\nabla_{\perp} v_{||}$, to $\mathbf{v}$ at each point in our computational box. Distribution functions, $PF_q(x)$, of each quantity, q, are compiled and moments calculated according to

$$M_n = \frac{\int_{-\infty}^{\infty} x^n PF_q(x)}{\left[\int_{-\infty}^{\infty} x^2 PF_q(x)\right]^{n/2}}. \tag{4.30}$$

These are tabulated below.

	Simulation Z45			Jiminez et al.			Gaussian
n	v	$\nabla_{||} v_{||}$	$\nabla_{\perp} v_{||}$	v	$\nabla_{||} v_{||}$	$\nabla_{\perp} v_{||}$	
3	0	-.43	0	0	-.50	0	0
4	1.6	4.4	5.9	2.8	4.6	6.19	3
5	0	-6.5	0	0	-8.0	0	0
6	3.4	48	102	13.0	55	110	15

Because our simulation is of decaying turbulence whereas that of Jiminez et al. is forced, appropriate comparisons are restricted to inner scale quantities derived from components of $\boldsymbol{\nabla}\mathbf{v}$ and exclude outer scale quantities derived from components $\mathbf{v}$. With this proviso, our results are in satisfactory agreement with theirs.

4.8 Simulation Design

We carry out simulations of both forced and decaying MHD turbulence. Delta-correlated forcing is implemented by adding a random forcing field of energy $\epsilon \Delta t$ to the existing fields each timestep, where ϵ is the specified forcing power. Fourier modes within 3 lattice units of the origin receive random divergenceless values corre-

sponding to a power spectrum of $E(s) \sim\sim s^{-5/3}$, with individual energies drawn from a Boltzman distribution. We force both velocity and magnetic fluctuations. Forcing $\mathbf{v}$ alone would artificially correlate the power received by $\mathbf{w}_\uparrow$ and $\mathbf{w}_\downarrow$.

The aspect ratio of our simulation box is chosen to match the anisotropy of the turbulence. In most of our simulations, $L_z \gg L_x = L_y$. We scale lengths to $L_z = 1$ and velocities to $v_A = 1$. Thus waves take $\Delta t = 1$ to propagate the length of the box. The excitation level, set by the parameter $(v_{L_\perp} L_z)/(v_A L_\perp)$, is chosen so that the longest waves cascade in less than $\Delta t = 1$. An equivalent statement is that a typical fieldline wanders by more than $L_\perp$ in the transverse direction during its passage across the length L_z of the box. This requires the excitation parameter to be somewhat larger than unity. Typical values in our simulations are of order 5. We generally run our simulations for a few crossing times. Thus nonlinear interactions are fully expressed on all scales.

Our basic procedure comes with a variety of refinements. The fields can be decomposed into their $\mathbf{w}_\uparrow$ and $\mathbf{w}_\downarrow$ components as given by equations (4.14). Each of these may be further separated into shear Alfvén and slow modes according to equations (4.15) and (4.16). In this manner we can selectively input and remove waves of any type and with any direction of propagation.

4.9 Catalog Of Simulations

A variety of simulations are referred to in §5. Each has an external magnetic field of unit strength aligned with the z-axis, uses a fourth order hyperviscosity, and is carried out in a box of dimensions $L_x = L_y = 2 \times 10^{-3}$, $L_z = 1$. The dimensionless forcing power is denoted by $\mathcal{P}$. It is chosen so that the rms dimensionless fluctuations of v and b have magnitude 3×10^{-3}. These values also characterize the initial states of simulations of decaying turbulence.

Simulation Parameters

ID	$(N_\perp, N_z)$	Δt	ν_4	Comments
Z114	$64, 256$	4×10^{-4}	5×10^{-37}	$\mathcal{P} = 2 \times 10^{-5}$
Z115	$128, 512$	3×10^{-4}	5×10^{-40}	$\mathcal{P} = 2 \times 10^{-5}$
Z117	$256, 512$	1.5×10^{-4}	5×10^{-43}	$\mathcal{P} = 2 \times 10^{-5}$
Z118	$128, 512$	3×10^{-4}	5×10^{-40}	$4 < s_\perp < 8$
Z119	$128, 512$	3×10^{-4}	5×10^{-40}	$8 < s_\perp < 16$
Z120	$128, 512$	3×10^{-4}	5×10^{-40}	$16 < s_\perp < 32$
Z121	$128, 512$	3×10^{-4}	5×10^{-40}	$2 < s_\perp < 4$
Z122	$128, 512$	3×10^{-4}	5×10^{-40}	$\mathcal{P} = 0$
Z123	$256, 512$	1.5×10^{-4}	5×10^{-43}	$32 < s_\perp < 64$
Z124	$256, 512$	1.5×10^{-4}	5×10^{-43}	$16 < s_\perp < 32$
Z125	$64, 256$	4×10^{-4}	5×10^{-40}	$\mathcal{P} = 0$
Z126	$128, 512$	3×10^{-4}	5×10^{-43}	$\mathcal{P} = 2 \times 10^{-5}$
Z127	$128, 512$	3×10^{-4}	5×10^{-43}	$\mathcal{P} = 2 \times 10^{-5}$
Z128	$64, 256$	4×10^{-4}	5×10^{-37}	$\mathcal{P} = 0$, $A \uparrow + S \downarrow$
Z129	$64, 256$	4×10^{-4}	5×10^{-37}	$\mathcal{P} = 0$, $A \uparrow + A \downarrow$

4.9.1 Simulations of Forced Turbulence

Our basic simulations include forcing at a total power per unit mass of $\mathcal{P} = 2 \times 10^{-5}$. Recall that $\rho = 1$ and $v_A = 1$. Statistically equal power is input into shear Alfvén and slow waves propagating in opposite directions along the magnetic field. Higher

resolution simulations run for shorter times are initialized by refining lower resolution simulations run for longer times.

Our sequence of forced simulations begins with **Z114** which has resolution $64 \times 64 \times 256$ and runs up to $t = 6.6$. Initial condition for simulations **Z115**, **Z126**, **Z127** with resolutions $128 \times 128 \times 512$ are drawn from **Z114** at $t = 2.4$, 4.7, and 6.6, respectively. These are times at which the fluxes of oppositely directed shear Alfvén waves in **Z114** nearly balance. The refined simulations run for an additional $\Delta t = 0.4$, long enough for small scale structure to develop up to the dealiasing cutoff. Our highest resolution, $256 \times 256 \times 512$, simulation **Z117** is initialized from **Z115** at $t = 2.8$ and run until $t = 2.95$.

4.9.2 Simulations of Decaying Turbulence

Our simulations of decaying turbulence are designed to test specific properties of the MHD cascades. Simulation **Z125** continues **Z114** without forcing from t=2.8 to t=9.9. Simulations **Z128** and **Z129** are initialized from **Z114** at $t = 6.6$, the former by removing the Alfvén down and slow up waves and the latter by removing all slow waves. A series of simulations are initialized from forced simulations by removing all upward propagating waves outside a specified band while leaving the down modes unchanged. Simulations **Z121**, **Z118**, **Z119**, and **Z120** are each initialized from **Z115** at t=2.8 with the up modes band-filtered from $2 \leq s_\perp \leq 4$, $4 \leq s_\perp \leq 8$, $8 \leq s_\perp \leq 16$, and $16 \leq s_\perp \leq 32$, respectively. Likewise, simulations **Z124** and **Z123** are initialized from **Z117** at t=2.95 with up modes band-filtered from $16 \leq s_\perp \leq 32$ and $32 \leq s_\perp \leq 64$, respectively. The former has the same up band as **Z120** but twice the transverse resolution.

Chapter 5 SIMULATION RESULTS

5.1 Power Spectra

We obtain power spectra from our simulations as described in §4.4.

5.1.1 1D Power Spectra

Examples of 1D power spectra obtained by averaging results from three simulations (Z115, Z126, and Z127) of resolution $128 \times 128 \times 512$ are presented in Figure 5.1. Each spectrum has an inertial range slope of approximately 1.5. The power spectra displayed in Figure 5.2 come from a single simulation (Z117) with resolution $256 \times 256 \times 512$. Aside from their extended inertial ranges, they look similar to those plotted in Figure 5.1.

5.1.2 2D Power Spectra

Figure 5.3 displays a sequence of 1D power spectra made by taking cuts parallel to the s_z axis across the 2D power spectrum of shear Alfvén waves from simulation Z117. Note that there is negligible power at the highest s_z even for the highest $s_\perp$. Thus this simulation has adequate resolution along the z direction, something we verify for each of our simulations. As we emphasize in §4.3 and §4.4, these cuts do *not* suffice to determine the structure of turbulence parallel to the local magnetic field. For that we need to use structure functions (see §5.2).

5.2 Structure Functions

Figure 5.4 displays transverse and longitudinal structure functions for both shear Alfvén and slow waves calculated as described in §4.5 from data obtained by averaging

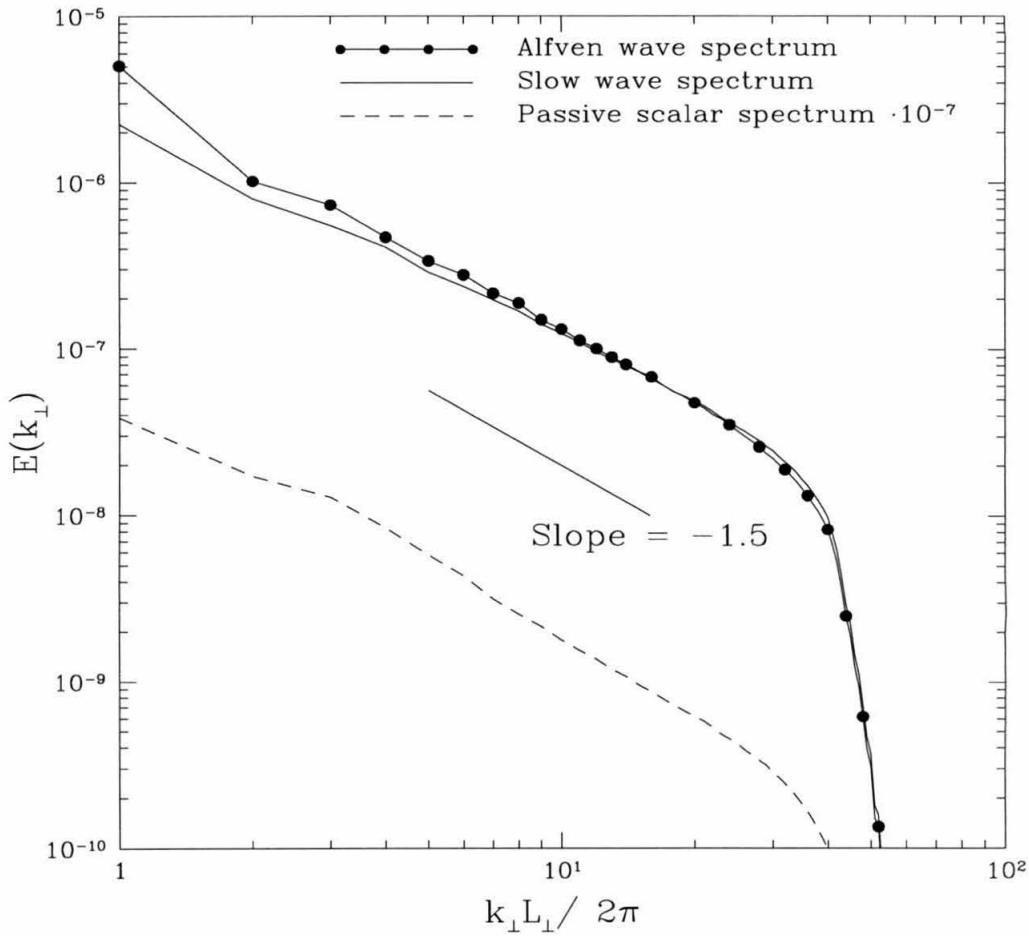

Figure 5.1: *1D Averaged Power Spectra.*

Energy spectra obtained by averaging results from simulations Z115, Z126, and Z127 with resolution $128 \times 128 \times 256$.

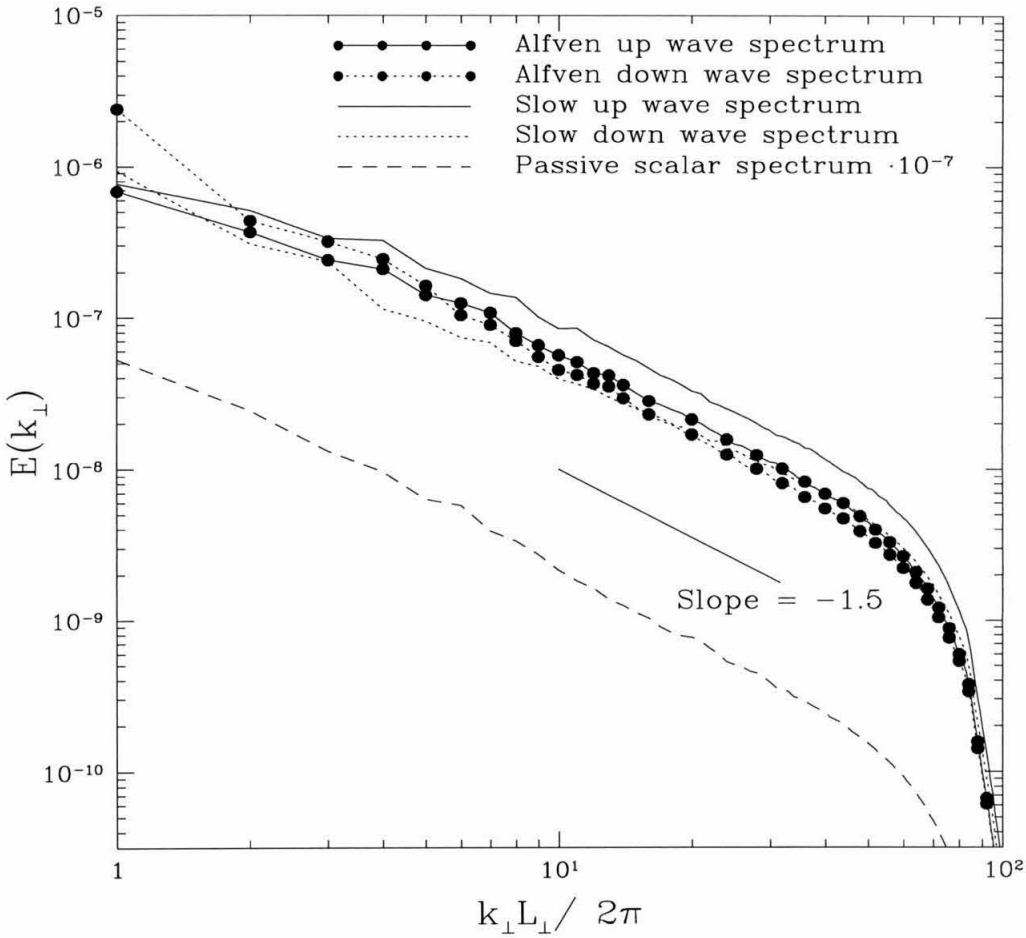

Figure 5.2: *Highest Resolution 1D Power Spectra.*

Energy spectra obtained from simulation Z117 with resolution $256 \times 256 \times 512$.

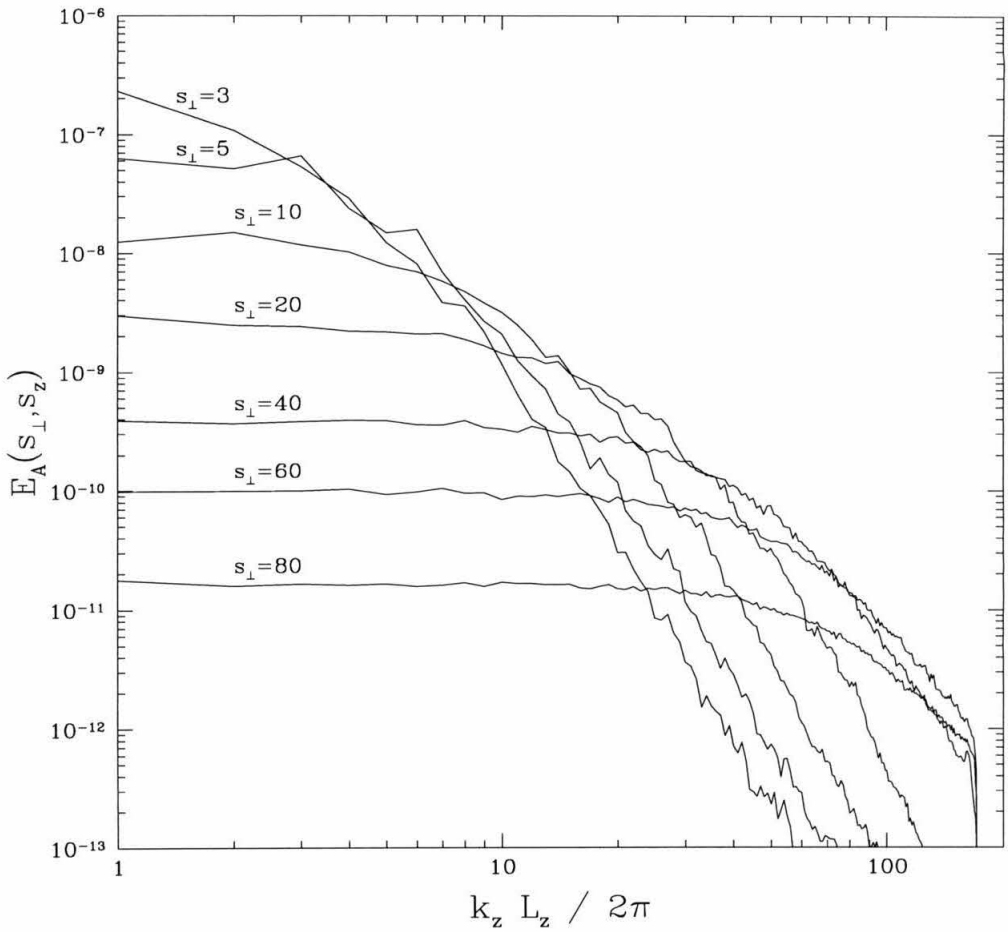

Figure 5.3: *Cuts Across 2D Power Spectrum.*

The Alfvén energy spectrum as a function of s_z at fixed $s_\perp$ from simulation Z117.

results from simulations Z115, Z126, and Z127. The plots are truncated at $\lambda/L = 0.5$ because at greater separations the structure functions are affected by the application of periodic boundary conditions.

5.2.1 Anisotropy

Structure functions are the best measure of the scale dependent anisotropy of an MHD cascade. Ordered pairs of $\lambda_{||}$ and $\lambda_{\perp}$ obtained by equating the longitudinal and transverse structure functions for shear Alfvén waves shown in Figure 5.4 are plotted in Figure 5.5. We leave it to the reader to judge the degree to which this supports the prediction by GS that $\lambda_{||} \propto \lambda_{\perp}^{2/3}$ in the inertial range.

5.2.2 Ratio of Nonlinear to Linear Time Scales

The quantity $\chi = (\lambda_{\perp} v_A)/(\lambda_{||} v_{\lambda_{\perp}})$ is the ratio of the nonlinear to linear timescale associated with wave packets of dimensions $(\lambda_{\perp}, \lambda_{||})$. To evaluate χ we take $v_{\lambda_{\perp}} = SFT_A^{1/2}(\lambda_{\perp})$ from Figure 5.4 and $\lambda_{\perp}/\lambda_{||}$ from Figure 5.5. The plot in Figure 5.6 establishes that χ maintains a value near unity throughout the inertial range.

5.3 Energy Loss

Total, mechanical plus magnetic, energy is conserved in the inertial range of MHD turbulence. It is lost from high $k_{\perp}$ modes by a combination of hyperviscous dissipation and dealiasing.[1] Neither represents reality, but we hope that their effects do not compromise inertial range dynamics. Figure 5.7 includes plots from simulation Z115 of the hyperviscous and dealiasing energy losses per computational timestep. For reference, the total power spectrum is also displayed. Hyperviscous dissipation dominates dealiasing except at the highest $k_{\perp}$ where the residual power is negligible. This situation is typical of all our simulations.

[1] Energy is lost during dealiasing when we set the amplitudes of modes with $|s_{\alpha}| > N_{\alpha}/3$ to zero.

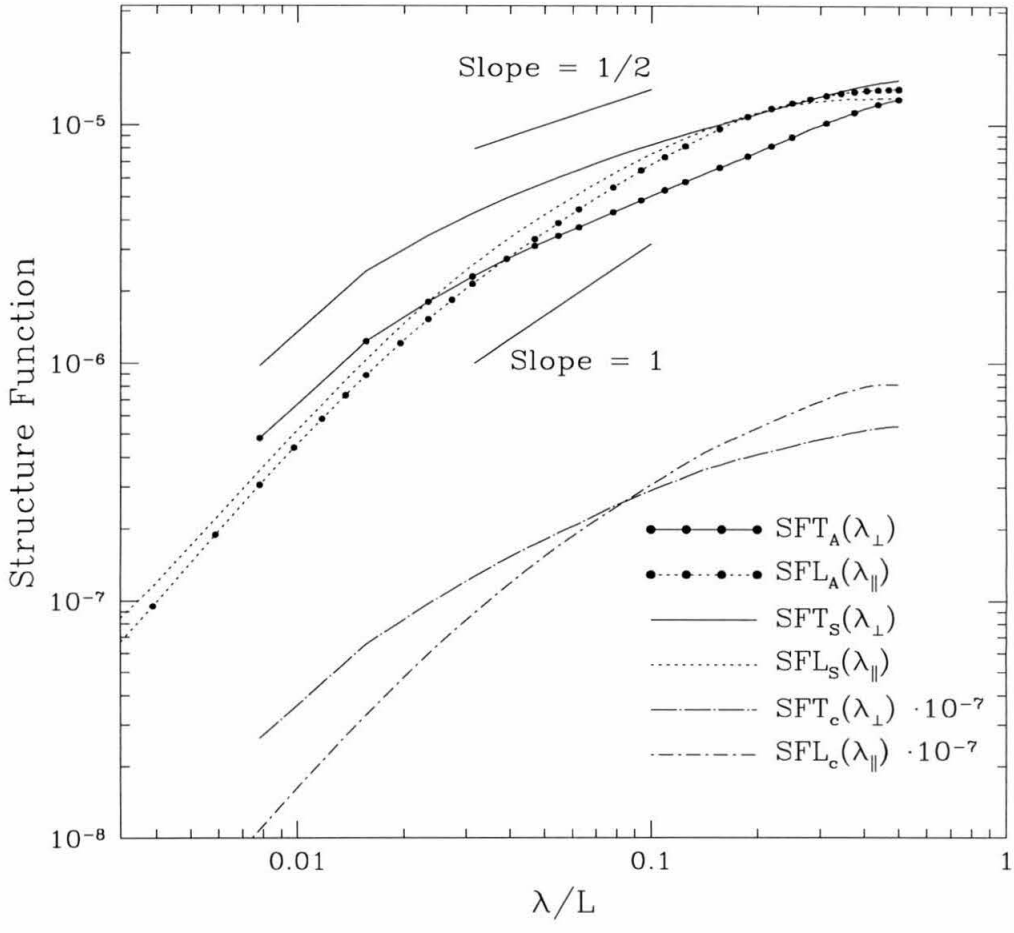

Figure 5.4: *Transverse and Longitudinal Structure Functions.*

Structure functions transverse and longitudinal to the local magnetic field direction are obtained by averaging results from simulations Z115, Z126, and Z127 with resolution $128 \times 128 \times 256$.

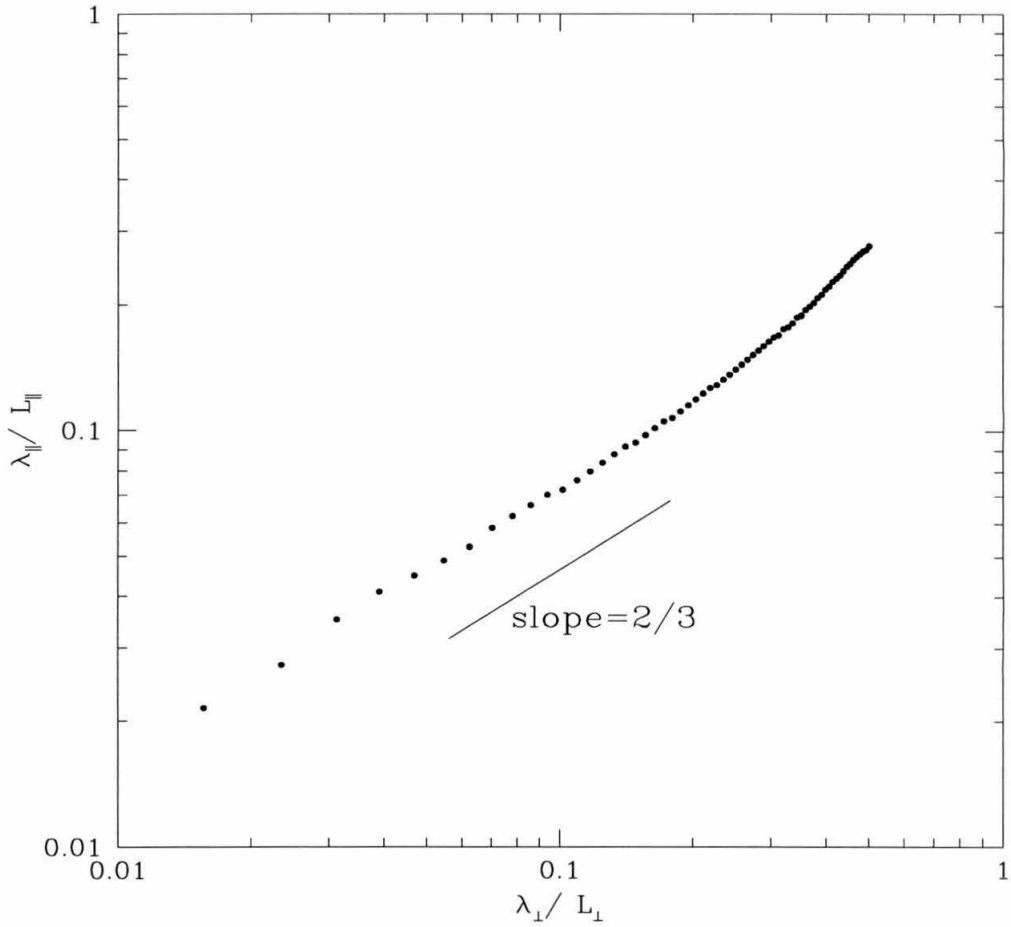

Figure 5.5: *Ordered Pairs of* $\lambda_{\perp}$ *and* $\lambda_{||}$.

Anisotropy of MHD turbulence is quantified by plotting values of $\lambda_{\perp}$ *and* $\lambda_{||}$ *obtained by setting* $SFT_A(\lambda_{\perp}) = SFL_A(\lambda_{||})$ *using the data displayed in Figure 5.4.*

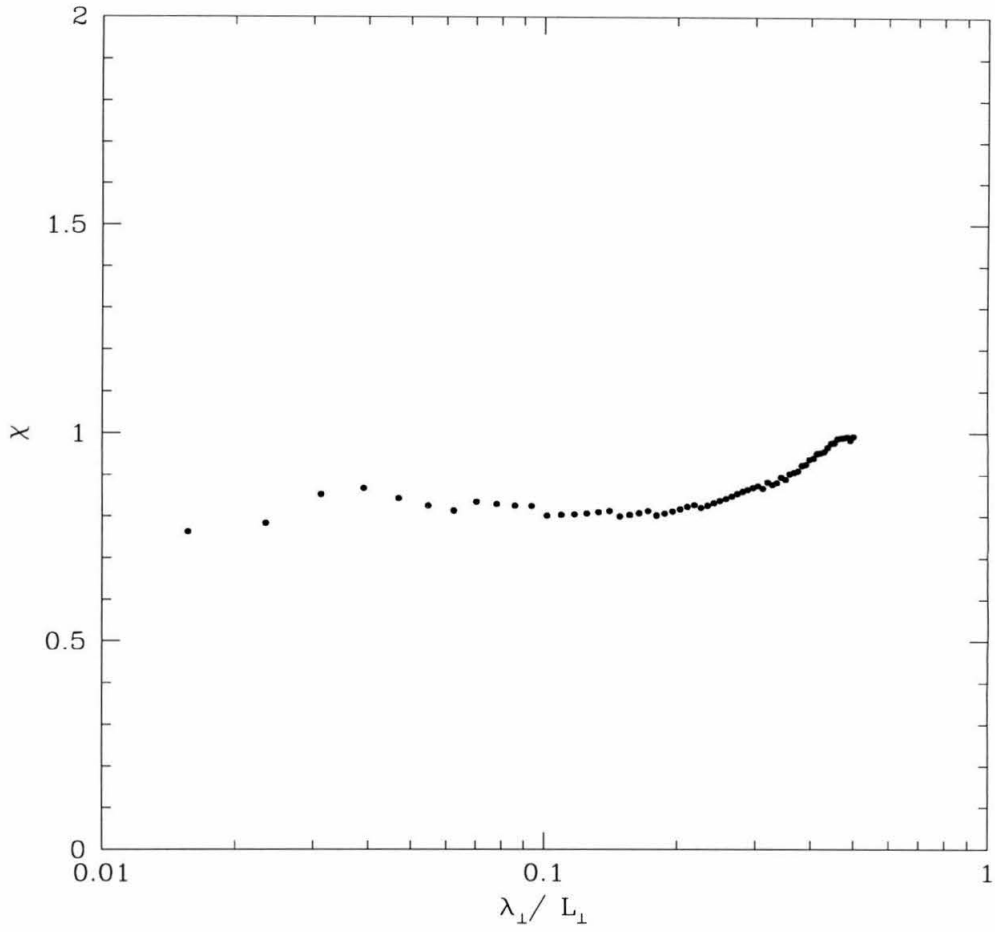

Figure 5.6: *Critical Balance.*

Data from Figures 5.4 and 5.5 are combined to form χ, the ratio of linear to nonlinear time scales. Note that χ has a nearly constant value close to unity throughout the inertial range. This confirms that MHD turbulence maintains a state of critical balance.

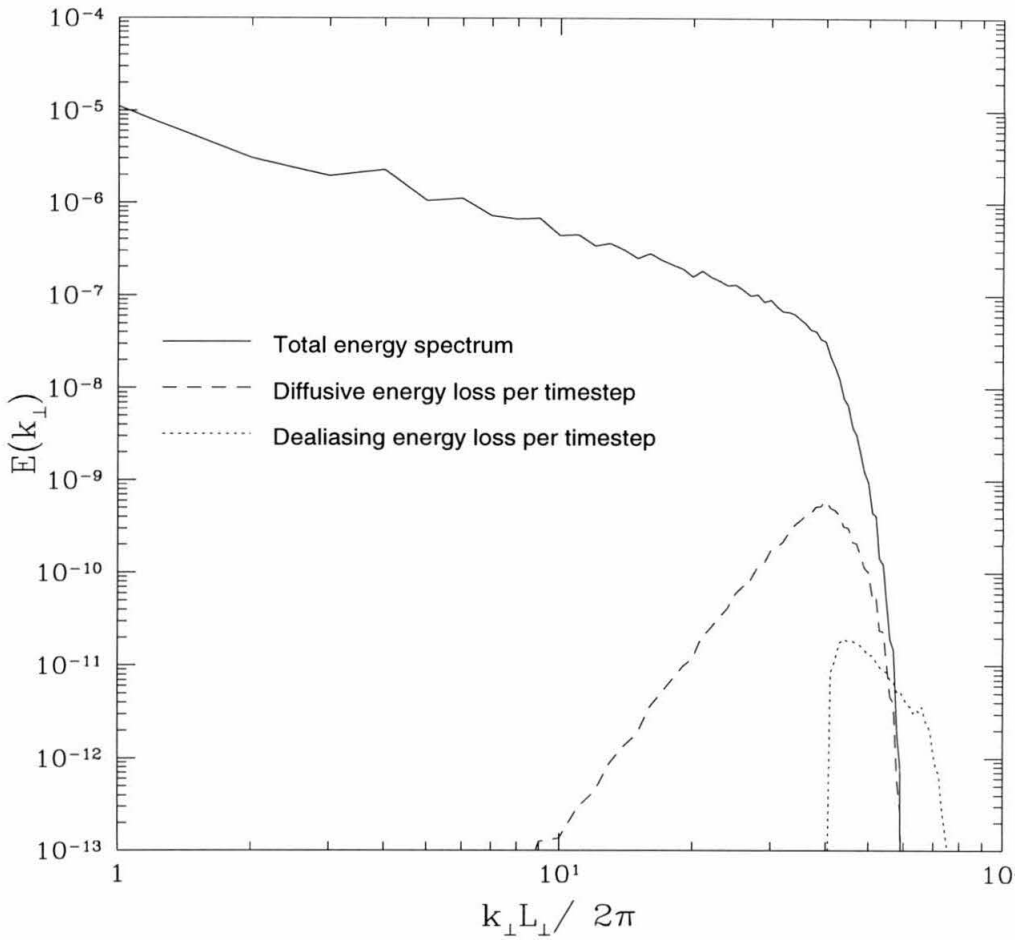

Figure 5.7: *Energy Loss Per Timestep by Hyperviscous Dissipation and Dealiasing.*

Energy is lost from high $k_\perp$ modes by hyperviscous dissipation and dealiasing. The former dominates the latter when integrated over the spectrum. Neither is significant in the inertial range. The results shown here are from simulation Z115.

5.4 Imbalance

Because only oppositely directed waves interact, turbulent cascades tend to become unbalanced. By unbalanced, we mean that unequal fluxes of energy propagate in opposite directions along the magnetic field.

5.4.1 Forced Turbulence

Mode energies from simulation Z114 of forced turbulence with resolution $64 \times 64 \times 256$ are plotted as a function of time in Figure 5.8.[2] Characteristic fluctuations of order unity occur on a time scale $\Delta t = 1$. Imbalance appears to saturate on longer time scales.

5.4.2 Decaying Turbulence

Imbalance is more severe in decaying turbulence. Figure 5.9 displays energies of individual modes as a function of time obtained from simulation Z125 of resolution $64 \times 64 \times 256$. The initial imbalance increases without limit.

5.5 Passive Role Of Slow Waves

5.5.1 Cascading Of Slow Waves By Shear Alfvén Waves

Simulation Z128 of decaying turbulence with resolution $64 \times 64 \times 256$ is designed to assess the mutual effects of shear Alfvén waves on slow waves and vice versa. We initialize it by removing the upward propagating slow waves and the downward propagating shear Alfvén waves from simulation Z114 at $t = 6.6$. It is then run for $\Delta t = 1$. Figure 5.10 illustrates the evolution of the energies in upward propagating shear Alfvén waves and downward propagating slow waves. The only change in the spectrum of shear Alfvén waves is a decay at large $k_\perp$ which is entirely attributable to energy loss by hyperviscosity and dealiasing. By contrast, the spectrum of slow

[2] This simulation is the source of initial conditions for many higher resolution simulations.

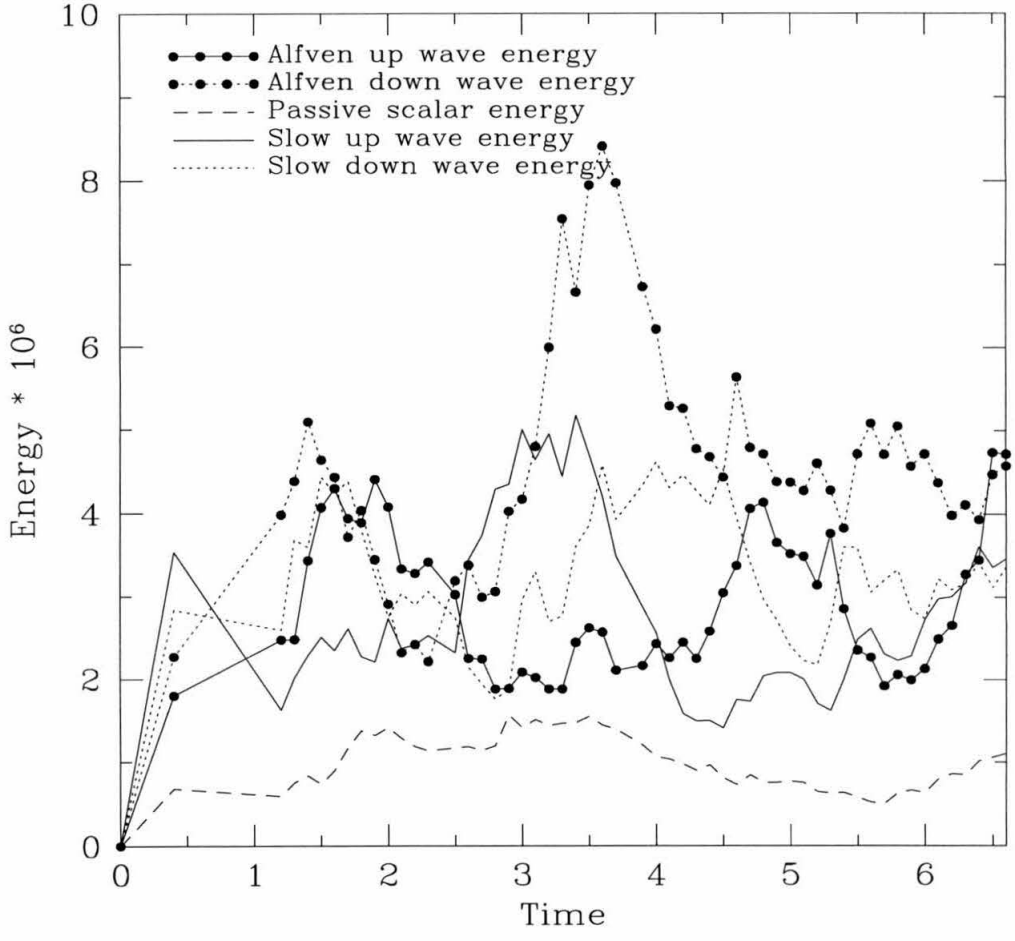

Figure 5.8: *Forced Turbulence.*

Mode energies as a function of time for forced turbulence from simulation Z114 of resolution $64 \times 64 \times 256$.

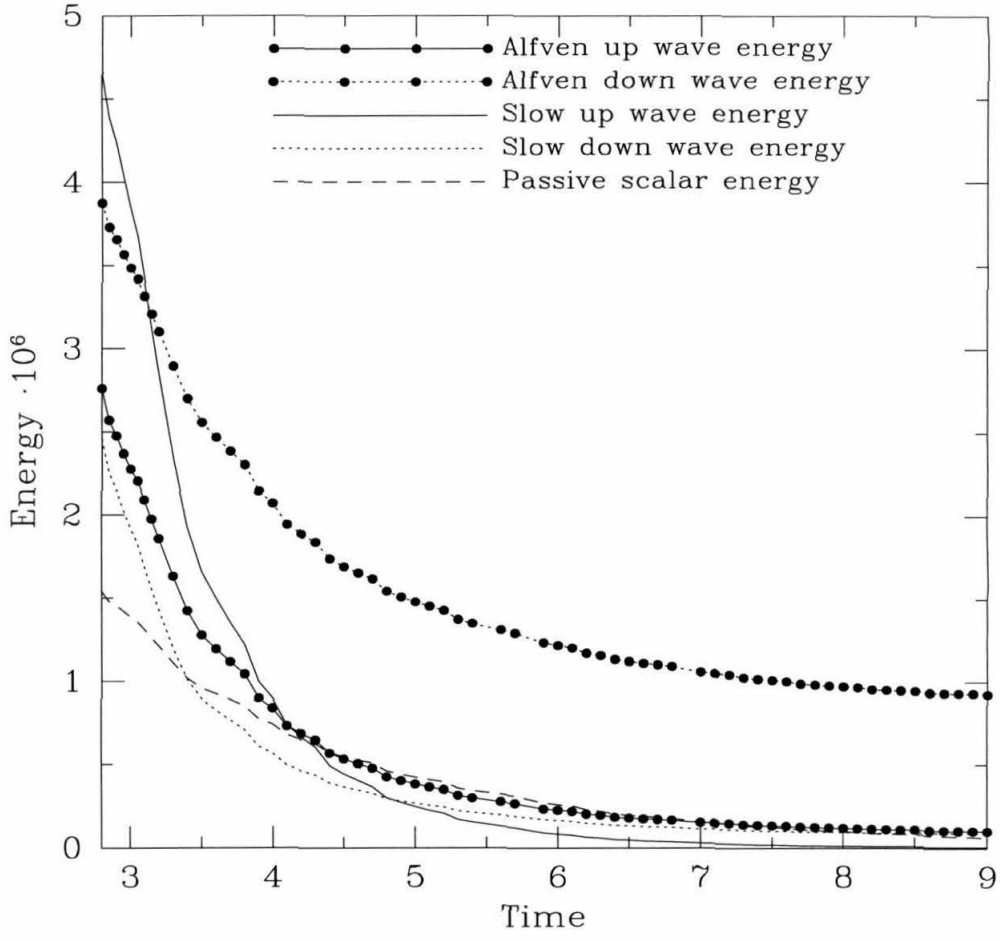

Figure 5.9: *Decaying Turbulence.*

Energy as a function of time for shear Alfvén and slow modes in decaying turbulence. The simulation is Z125 with resolution $64 \times 64 \times 256$.

waves decays at all $k_\perp$ at a rate consistent with that shown in Figure 5.9. These findings demonstrate that shear Alfvén waves control the MHD cascade and that the slow waves play a passive role.

5.5.2 Conversion Of Shear Alfvén Waves To Slow Waves

Simulation Z129 of decaying turbulence with resolution $64 \times 64 \times 256$ is tailored to measure the rate at which shear Alfvén waves are converted into slow waves. It is initialized from Z114 at $t = 6.6$ by removing all slow waves and then run for $\Delta t = 1$. As demonstrated by Figure 5.11, at the end of this interval, which corresponds to about a decay time at the outer scale (see Fig. 5.9), the slow waves carry negligible energy. The small admixture shown may result from the limited ability of our scheme of spectral decomposition to distinguish slow waves from shear Alfvén waves as discussed in §4.3.

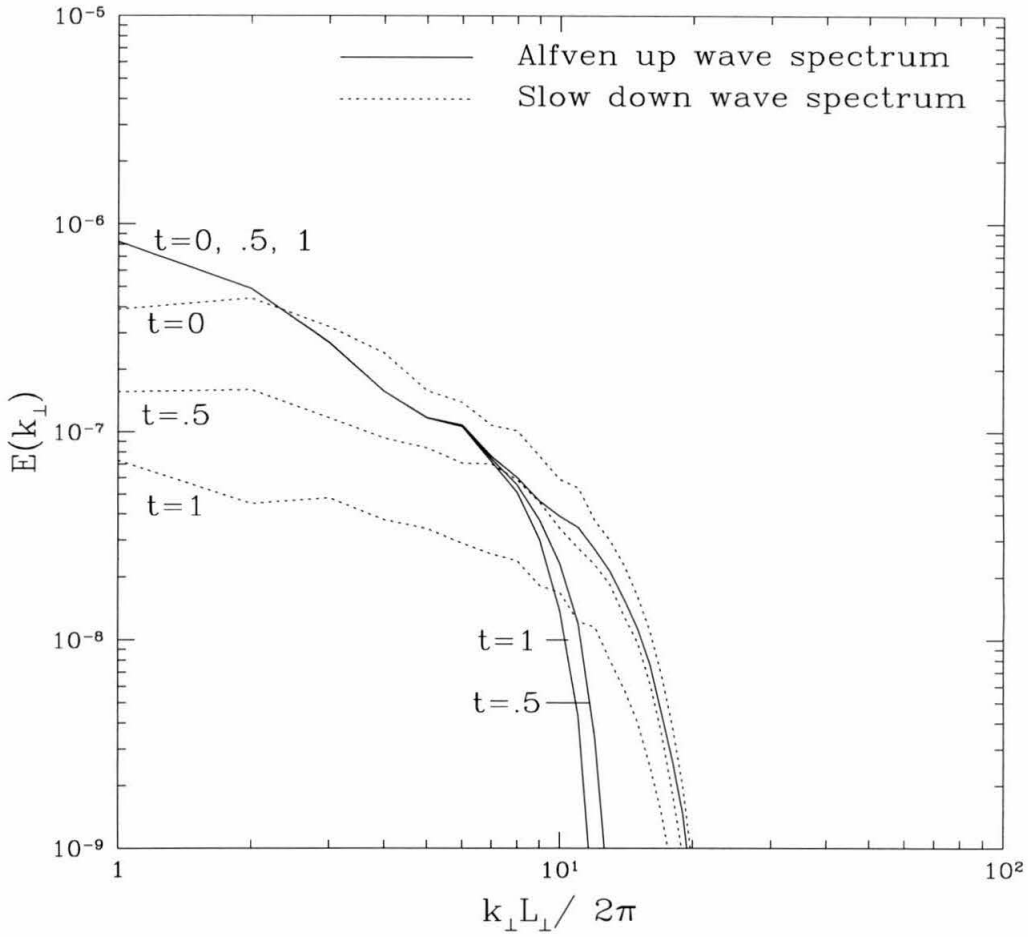

Figure 5.10: *Passive Role of Slow Waves.*

Upward moving shear Alfvén waves interact with downward moving slow waves. The power spectrum of the former decays only at large $k_\perp$ whereas that of the latter decays at all $k_\perp$. Results are taken from simulation Z128 of decaying turbulence with resolution $64 \times 64 \times 256$.

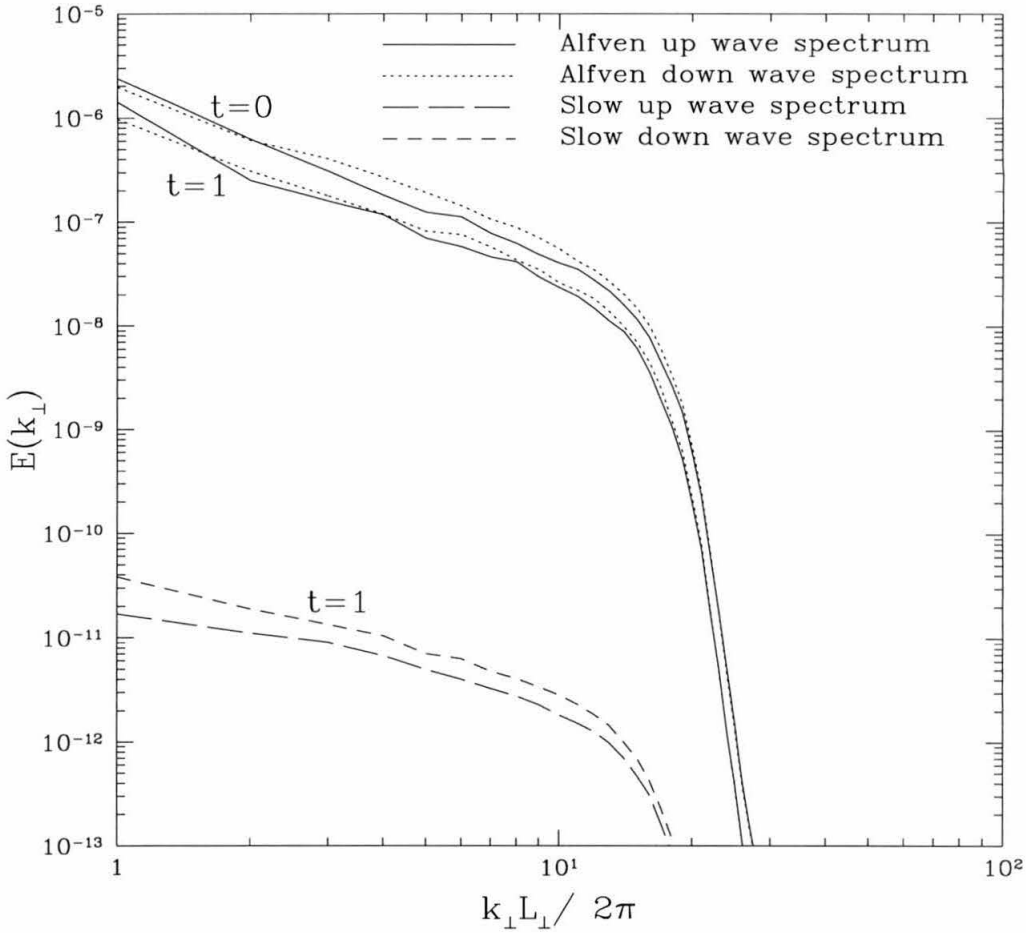

Figure 5.11: *Negligible Conversion of Shear Alfvén to Slow Waves.*

Slow wave production in a simulation of decaying turbulence initialized with pure shear Alfvén waves. After one decay time the slow waves contain $\lesssim 10^{-4}$ *of the total energy. This amount is indistinguishable from the false slow waves that our spectral decomposition procedure would report due to the tilt of the local magnetic field relative to the global z axis. Data plotted comes from simulation Z129 with resolution* $64 \times 64 \times 256$.

5.6 Cascade Diagnostics

We design special simulations to exploit the fact that only oppositely directed waves interact. Each of these is initialized by removing all but a narrow band in $k_\perp$ of up waves from a fully developed forced simulation. These are then run without forcing so that we can observe the evolution of the energy in the up band as it spreads into adjacent bands. Since the down waves evolve weakly, we restrict the lengths of these runs to $\Delta t = 1/2$ so that interactions do not repeat.

Initial conditions for simulations Z121, Z118, Z119, and Z120 are provided by band-filtering simulation Z115 at $t = 2.8$ with up modes retained from $2 \leq s_\perp \leq 4$, $4 \leq s_\perp \leq 8$, $8 \leq s_\perp \leq 16$, and $16 \leq s_\perp \leq 32$, respectively. Each of these simulations has resolution $128 \times 128 \times 512$. Resolution $256 \times 256 \times 512$ simulations Z124 and Z123 are initialized from simulation Z117 by band-filtering at t=2.95 with up modes retained from $16 \leq s_\perp \leq 32$ and $32 \leq s_\perp \leq 64$, respectively.

5.6.1 Absence Of An Inverse Cascade

Figure 5.12 summarizes how energy spreads from each of selected band into adjacent bands. It establishes that the predominant movement is toward higher $k_\perp$. There is no evidence for an inverse cascade. A more detailed demonstration for the selected band $8 \leq s_\perp \leq 16$ is provided in Figure 5.13 which is based on simulation Z119.

5.6.2 Resolution Dependence

Figure 5.14 compares results from simulation Z120 of resolution $128 \times 128 \times 256$ with those from simulation Z124 of resolution $256 \times 256 \times 512$. Each simulation is initialized with energy in up waves confined to the band $16 \leq s_\perp \leq 32$. Note how well the energies in the central and left-hand bands from the two simulations match as they evolve. This establishes that the largest $k_\perp$ band in simulation Z120 is a valid part of the inertial range.

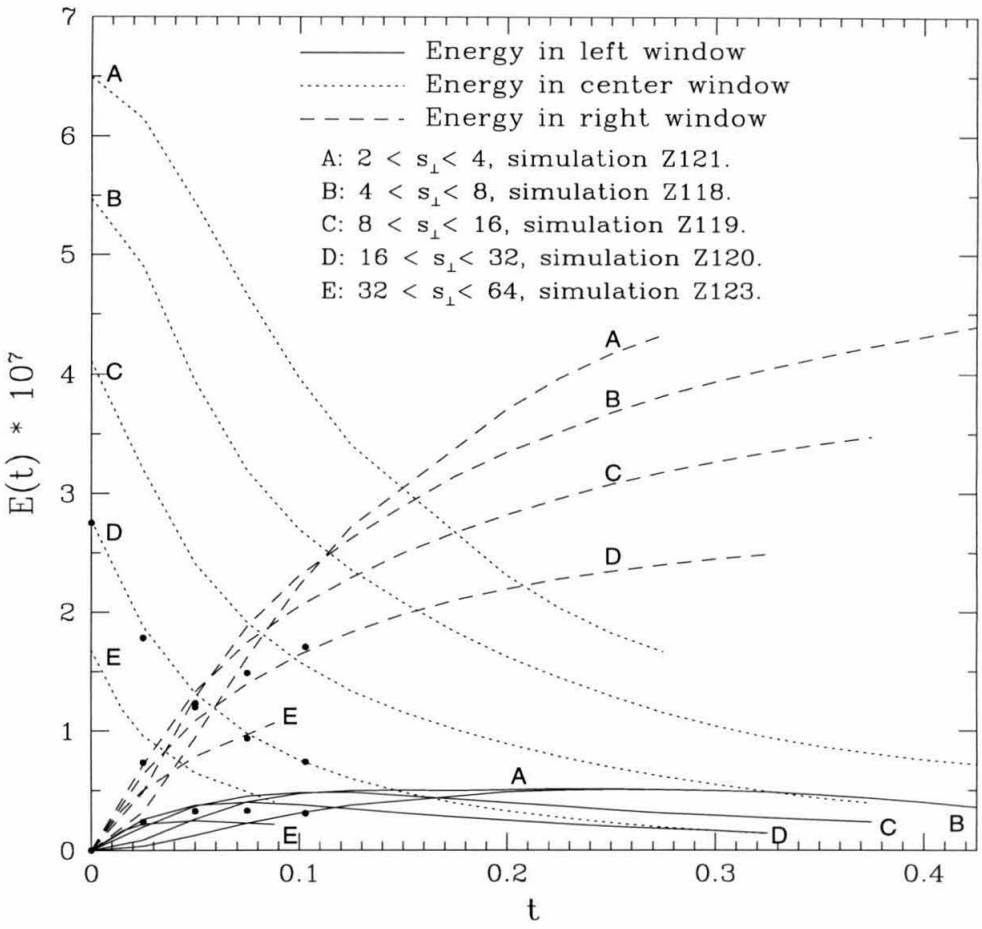

Figure 5.12: *Summary of Bandpass Filtered Simulations.*

We plot the energy as a function of time in the center band and in the bands immediately to its left and right for each bandpass filtered simulation. Points correspond to simulation Z124, which is initialized with the same up mode band as simulation Z120 but with twice the transverse resolution in the down modes. There is good agreement between simulations Z120 and Z124 as shown in more detail in Figure 5.14.

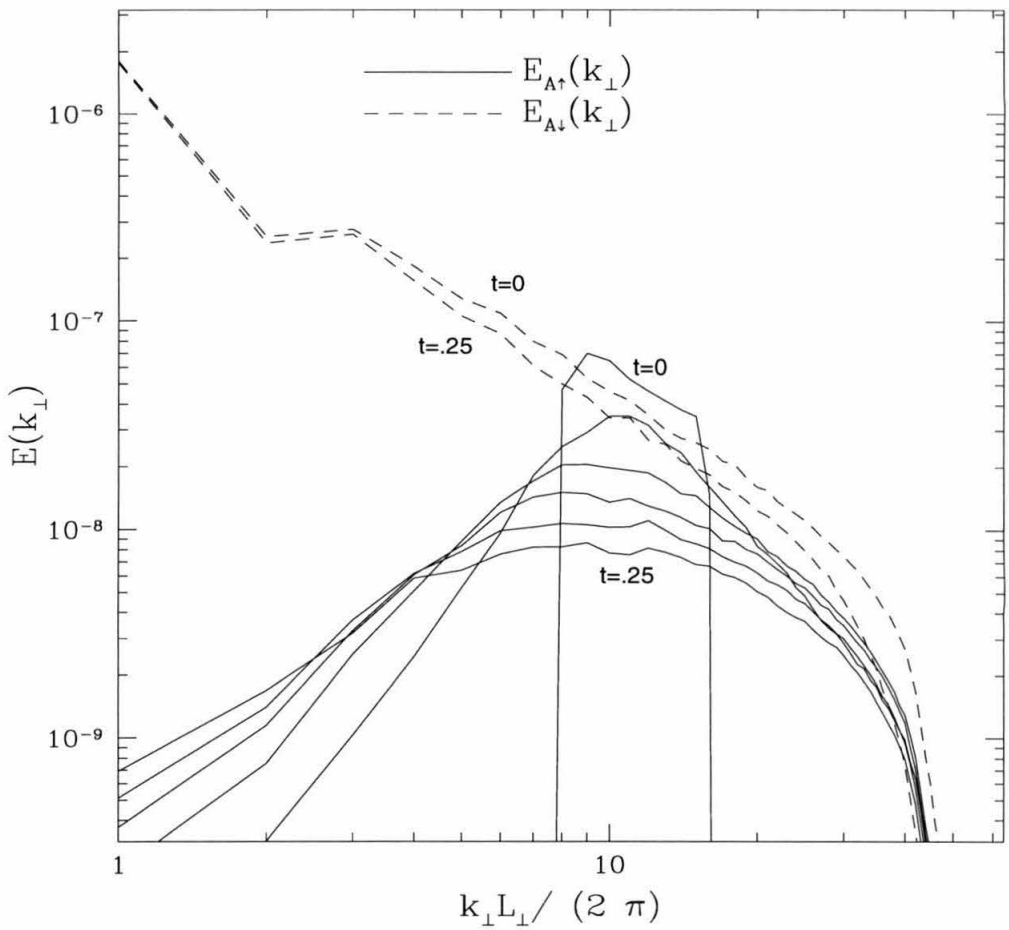

Figure 5.13: *Absence of an Inverse Cascade.*

Dashed lines depict the initial and final down wave spectra. The up wave spectra are plotted at a succession of times differing by $\Delta t = .05$. *Almost all of the energy that leaves the band* $8 \leq s_\perp \leq 16$ *moves to higher* $s_\perp$. *These data are taken from simulation Z119.*

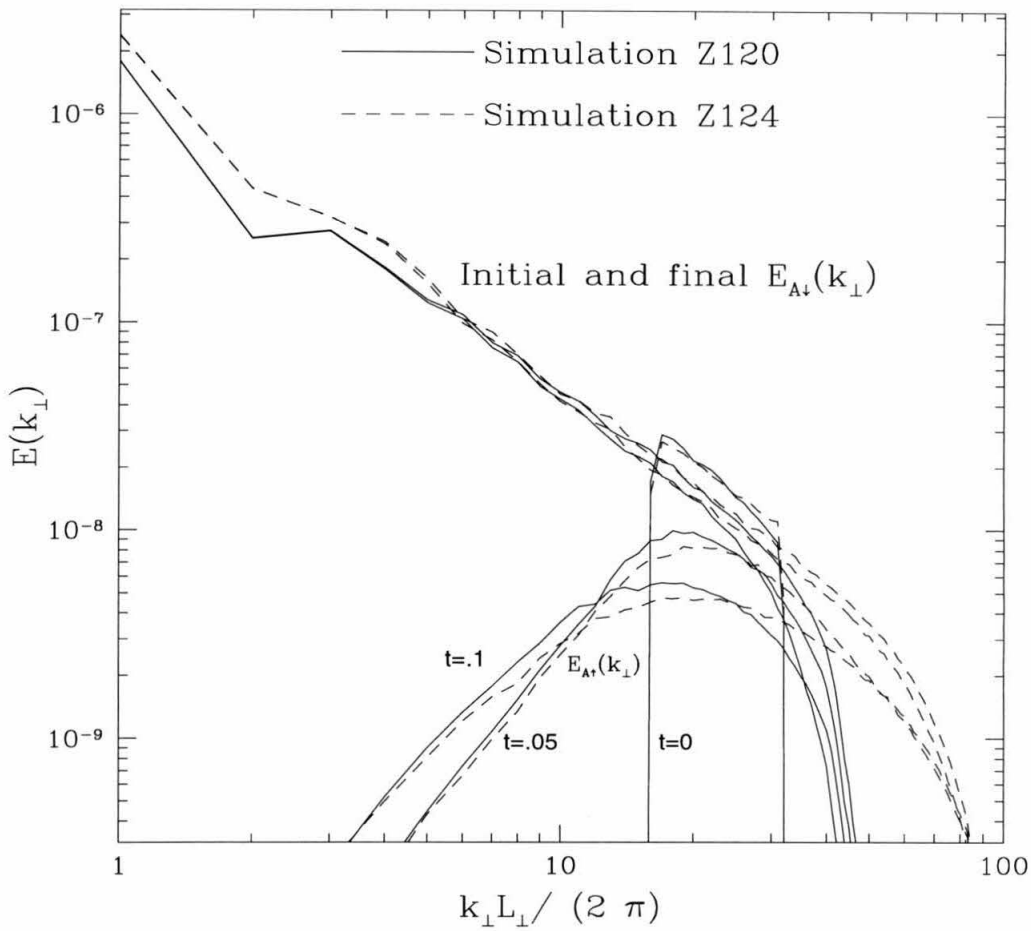

Figure 5.14: *Comparison of Simulations at Different Resolution.*

Increased resolution has little effect on the evolution of energy in the left-hand and central bands. Thus the latter resides in the inertial range in even the lower resolution simulation. Energy which moves into the right-hand band is more rapidly dissipated in the lower resolution simulation and more effectively stored in the higher resolution one.

5.6.3 Cascade Time

As a standard measure of the time scale for energy transfer across $\lambda_\perp$, we take $t_c \sim \lambda_\perp / v_{\lambda_\perp}$, where $v_{\lambda_\perp}$ is obtained from the transverse structure functions of downward propagating Alfvén waves according to $2v_{\lambda_\perp}^2 = SFT_{A\downarrow}(\lambda_\perp)$. An alternative definition suitable for band-filtered simulations determines $v_{\lambda_\perp}^2$ by integrating the power spectrum of downward propagating shear Alfvén waves over the interval $k_{\perp\min} \leq k_\perp \leq k_{\perp\max}$ of the central band of the upward propagating waves. We denote this form of the cascade time by $t_{c'}$. Banded simulations also permit a more direct measure of the cascade time as that at which the energy in the right-hand band matches that in the central band. We identify this version by the symbol t_h.

Values for the different types of cascade time are tabulated below. Even for the lowest $k_\perp$ band, each is substantially smaller than the time, $\Delta t = 1$, that waves take to cross the computational box.

CASCADE TIMES

$s_\perp$	$\lambda_\perp / L_\perp$	$v_\perp$	$v'_\perp$	$t_c = \lambda_\perp / v_\perp$	t_h	t_h/t_c	$t_h/t_{c'}$
2-4	.188	$3.28 \cdot 10^{-3}$	$1.20 \cdot 10^{-3}$	.115	.165	1.43	.53
4-8	.094	$2.67 \cdot 10^{-3}$	$1.07 \cdot 10^{-3}$	.070	.140	2.00	.80
8-16	.047	$2.10 \cdot 10^{-3}$	$.84 \cdot 10^{-3}$	.045	.100	2.22	.85
16-32	.023	$1.58 \cdot 10^{-3}$	$.67 \cdot 10^{-3}$	.029	.075	2.59	1.09
32-64	.0117	$1.29 \cdot 10^{-3}$	$.53 \cdot 10^{-3}$	.0181	.060	3.31	1.36

For ease of comparison, we plot the tabulated values against $k_\perp L_\perp / (2\pi)$ in Figure 5.15. Slopes exhibited by t_c and t'_c are similar, but t_h declines much more slowly with increasing $k_\perp$.

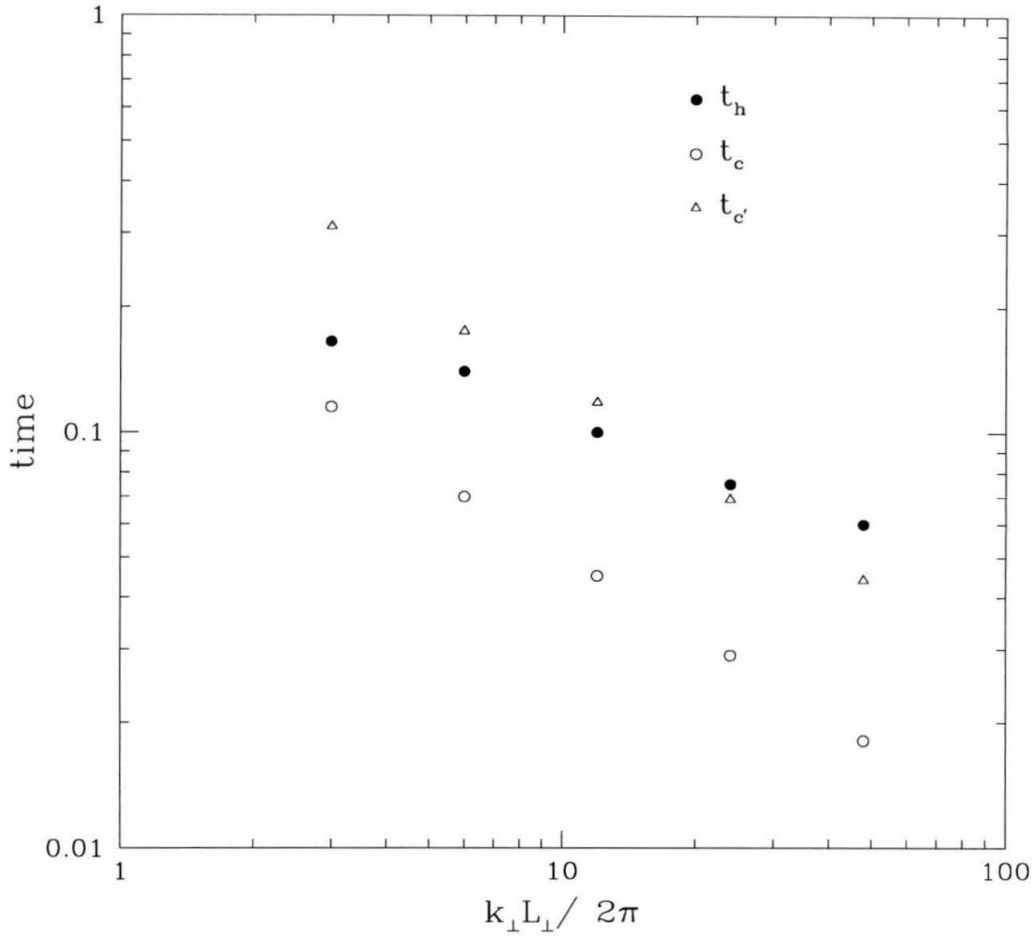

Figure 5.15: *Cascade Times.*

A comparison of cascade times based on different definitions. See text for details.

5.7 Intermittency

Simulations of hydrodynamic turbulence exhibit structure that is not seen in random phase realizations of velocity fields with identical power spectra (Jiminez et al. 1993). We find the same to be true for MHD turbulence. This is illustrated in Figures 5.16-5.19. The left-hand panels display magnitudes of the curls of upward and downward propagating shear Alfvén and slow waves in a (x, y) slice at $z = 0$ taken from simulation Z117. Randomizing the phases of the Fourier coefficients used to generate the left-hand panels yields the images shown in the right-hand panels. Coherent structures, which are conspicuous in the former, are absent in the latter.

While the eye does an excellent job of recognizing intermittency, it is helpful to have a quantitative measure. To accomplish this, we apply a sequence of high-pass and low-pass filters to the Fourier coefficients used to generate Figures 5.16-5.19. A filter is identified by a value of $s_\perp$. High-pass filters remove modes with smaller $s_\perp$ and low-pass filters remove those with larger $s_\perp$. The former target structure in the Elsasser fields and the latter that in their gradients. Given filtered data, we compute normalized fourth order moments of relevant quantities q according to

$$M_4(q) = \frac{\langle q^4 \rangle}{\langle q^2 \rangle^2}, \tag{5.1}$$

where angular brackets denote volume average.

Figure 5.20 displays moments of the Elsasser fields as a function $k_\perp$ for high-pass filtered data. Moments of gradients of the Elsasser fields as a function of $k_\perp$ for low-pass filtered data are plotted in Figure 5.21. For comparison, each figure includes moments obtained from the random phase versions of the corresponding simulations. It is worth noting that $M_4(q) = 1 + 2/n$ for data obeying n-dimensional Gaussian statistics, and that slow waves correspond to $n = 1$ and shear Alfvén waves to $n = 2$ in the limit $k_\perp \gg k_z$.

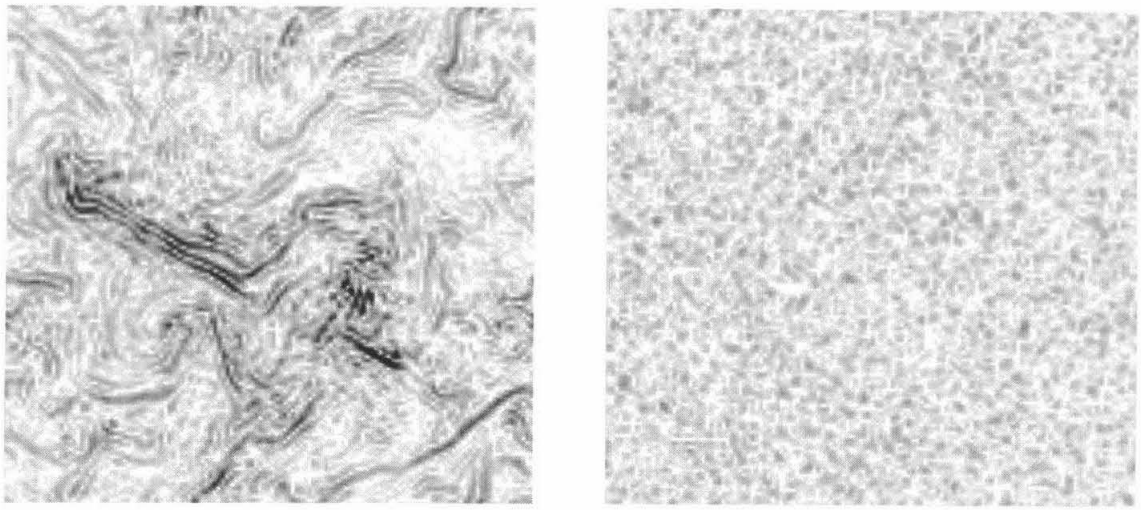

Figure 5.16: *Alfvén Up Modes.*

The left-hand panel shows a grey scale image of $|\nabla \times \mathbf{A}_{\uparrow}|$ *in a* (x, y) *slice at* $z = 0$. *For comparison, an image based on the same Fourier coefficients with random phases is shown in the right-hand panel.*

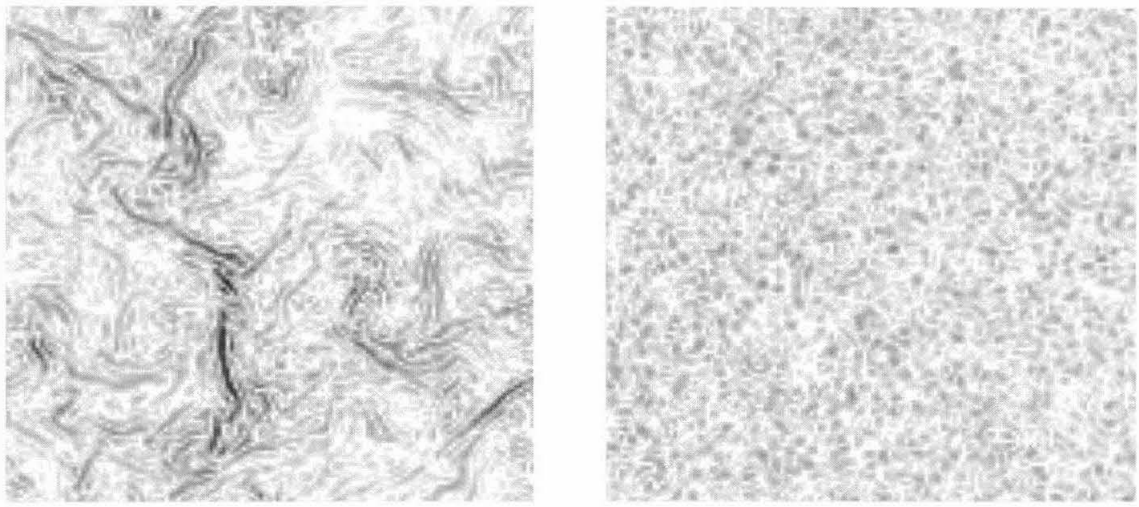

Figure 5.17: *Alfvén Down Modes.*

The left-hand panel shows a grey scale image of $|\nabla \times \mathbf{A}_{\downarrow}|$ *in a* (x, y) *slice at* $z = 0$. *For comparison, an image based on the same Fourier coefficients with random phases is shown in the right-hand panel.*

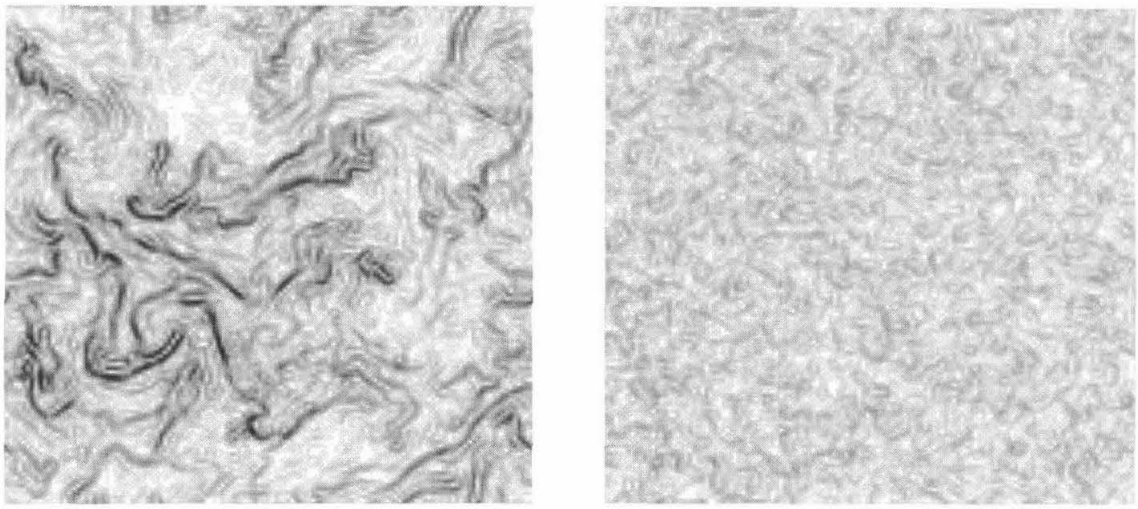

Figure 5.18: *Slow Up Modes.*

The left-hand panel shows a grey scale image of $|\boldsymbol{\nabla} \times \mathbf{S}_{\uparrow}|$ *in a* (x, y) *slice at* $z = 0$. *For comparison, an image based on the same Fourier coefficients with random phases is shown in the right-hand panel.*

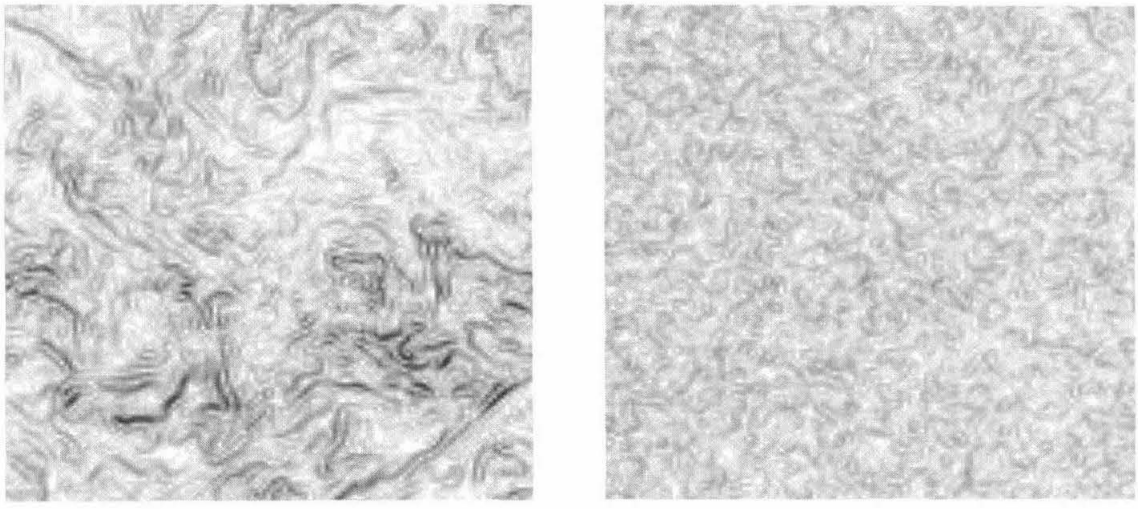

Figure 5.19: *Slow Down Modes.*

The left-hand panel shows a grey scale image of $|\boldsymbol{\nabla} \times \mathbf{S}_{\downarrow}|$ *in a* (x, y) *slice at* $z = 0$. *For comparison, an image based on the same Fourier coefficients with random phases is shown in the right-hand panel.*

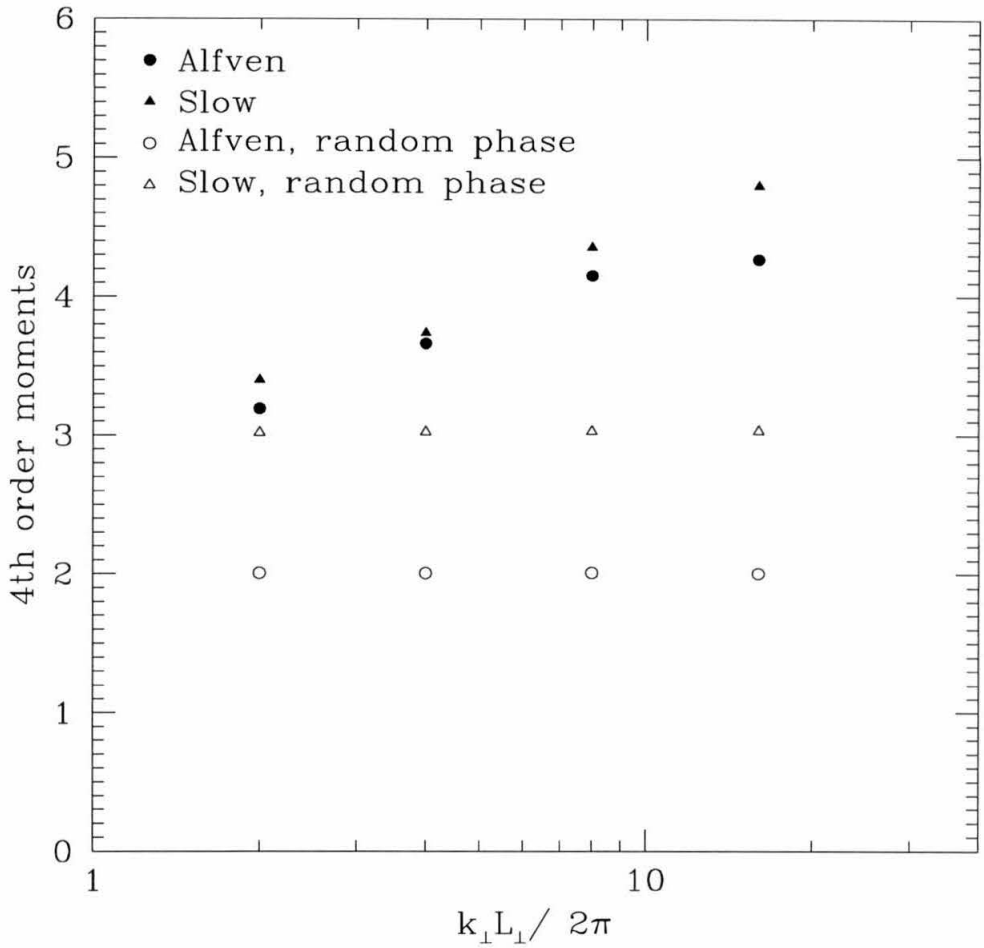

Figure 5.20: *Normalized 4th Order Moments for Alfvén and Slow Modes. Plotted points are average values of moments obtained from upward and downward propagating waves. The location of the high-pass filter is denoted by* $k_\perp$.

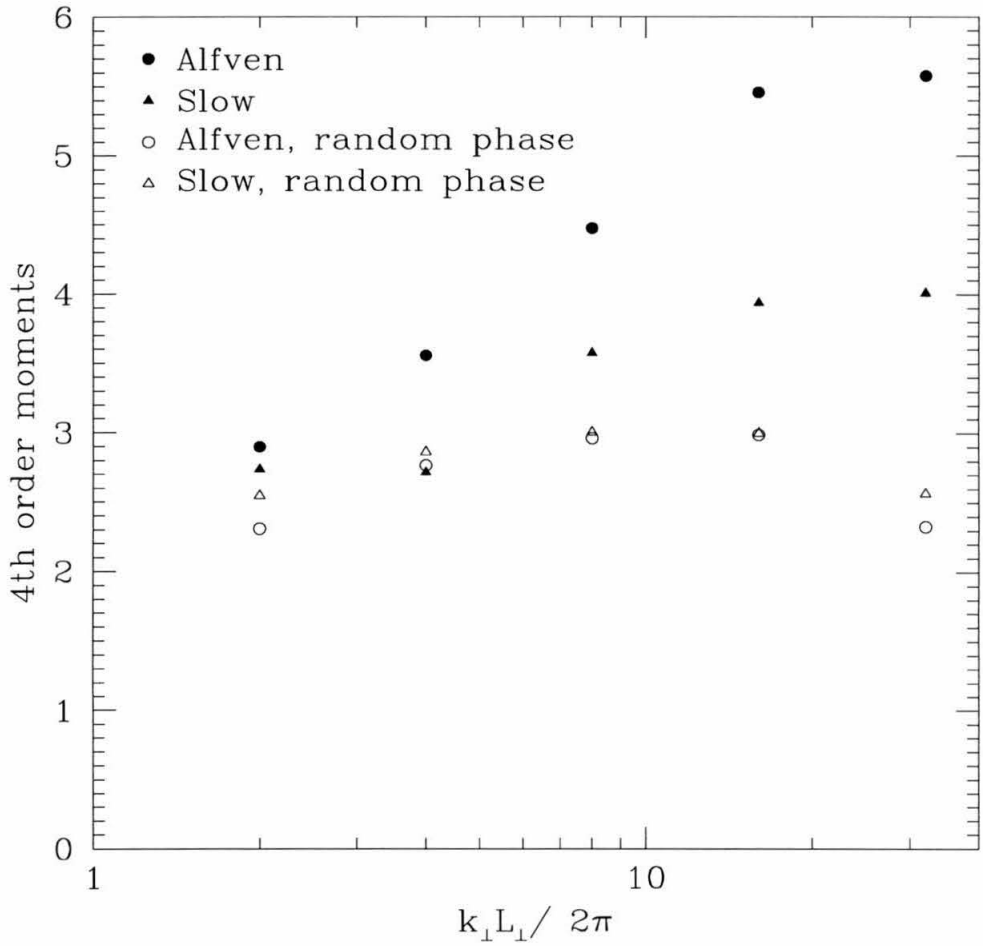

Figure 5.21: *Normalized 4th Order Moments from Gradients of Alfvén and Slow Modes.*

Gradients are defined as $\partial_x q$, where q is one of the Elsasser fields. Moments obtained from upward and downward propagating waves are averaged. The location of the low-pass filter is denoted by $k_\perp$.

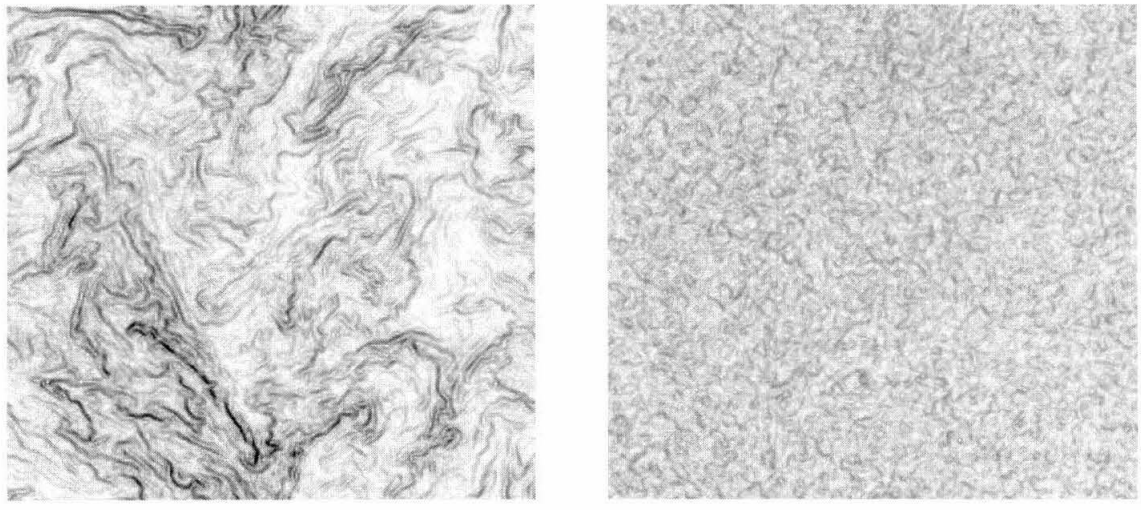

Figure 5.22: *Passive Scalar Gradient Magnitude.*

Passive scalar gradient magnitude, $|\nabla c|$, from our highest resolution, $256 \times 256 \times 512$, simulation Z117. The image plane is $z = 0$. Simulation data and its random phase transform are plotted in the left and right hand panels, respectively.

5.7.1 Passive Scalar

Intermittency also characterizes the concentration of the passive scalar. In the left and right hand panels of Figure 5.22, we plot the magnitude of the gradient of the passive scalar computed in our highest resolution simulation Z117. The contrast between the simulation and random phase data is striking. Coherent structures which are prominent in the former are absent from the latter.

Chapter 6 DISCUSSION OF RESULTS

6.1 Comparison With GS Model

6.1.1 Power Spectra and Structure Functions

The GSI model for the inertial range cascade of strong MHD turbulence is based on two assumptions.

1. Energy transfer is local in wavenumber space.

2. Linear and nonlinear time scales maintain near equality.

These assumptions lead to two predictions.

1. The 1D energy spectrum $E(\mathbf{k}_\perp) \propto k_\perp^{-5/3}$.

2. The cascade is anisotropic with energy confined within a cone $k_\parallel \propto k_\perp^{2/3}$.

Results from simulations presented in §5.1 and §5.2 agree with some aspects of the GS model and differ with others.

The 1D power spectra displayed in Figures 5.1 and 5.2 exhibit inertial range slopes, $m_{\rm ps}$, closer to $-3/2$ than to the $-5/3$ predicted in GSI. This is consistent with the slopes of the transverse structure functions $m_{\rm sf}$ shown in Figure 5.4 being close to $1/2$. Since power spectra and structure functions are related by Fourier transforms, these slopes should satisfy $m_{\rm ps} + m_{\rm sf} = -1$.

A clear increase of anisotropy with decreasing scale is demonstrated in Figure 5.5. It is consistent with the prediction by GSI that $\lambda_\parallel \propto \lambda_\perp^{2/3}$. Cho & Vishniac (2000) also observe this value in their simulations, although they use a different ratio of fluctuations to mean field.

Equality of linear and nonlinear time scales, also known as critical balance, predicts that $\lambda_\parallel / v_A \approx \lambda_\perp / v_{\lambda_\perp}$. Figure 5.6 shows that the ratio $\chi = (\lambda_\parallel v_{\lambda_\perp})/(\lambda_\perp v_A)$

maintains a value near unity throughout the inertial range as predicted in GSI. However, there is a marginal problem of consistency. Together, $\lambda_{\|} \propto \lambda_{\perp}^{2/3}$ and $\chi = \text{constant}$ imply $v_{\lambda_\perp} \propto \lambda_{\perp}^{1/3}$. But the transverse structure function from which we obtain $v_{\lambda_\perp}$ to use in forming χ yields $v_{\lambda_\perp} \propto \lambda_{\perp}^{1/4}$.

6.1.2 Passive Role of Slow Modes

The passive role played by slow waves in nearly transverse MHD cascades is neatly illustrated by Figure 5.10. GSII anticipates this behavior and offers a brief motivation. We provide an intuitive explanation in terms of field line geometry in §3.3.2. A mathematical derivation based on the equations of motion written in terms of Elsasser variables (eqn. [2.19]) is outlined below.

Consider the evolution of upward directed waves in a cascade whose anisotropy is measured by the scale dependent angle $\theta \approx k_{\|}/k_{\perp} \ll 1$. The nonlinear terms $\mathbf{w}_{\downarrow} \cdot \boldsymbol{\nabla} \mathbf{w}_{\uparrow}$ and $\boldsymbol{\nabla} P$ in equation (2.20) are responsible for their cascade. For comparable magnitudes of slow and shear Alfvén waves, $\mathbf{w}_d \cdot \boldsymbol{\nabla} \mathbf{w}_u$ is smaller by a factor θ if $\mathbf{w}_d \propto \mathbf{s}$ than if $\mathbf{w}_d \propto \mathbf{a}$. Here $\mathbf{s}$ and $\mathbf{a}$ are the unit polarization vectors of slow and shear Alfvén waves as defined in equation (2.18). Since the $\mathbf{w}_d \cdot \boldsymbol{\nabla} \mathbf{w}_u$ term is the sole source of P, the same comparison applies to the $\boldsymbol{\nabla} P$ term. Note that these comparisons hold for both shear Alfvén and slow $\mathbf{w}_u$ waves. As they are independent of the degree of nonlinearity, they apply to the intermediate MHD cascade as well as to the strong one.

6.1.3 Conversion Of Shear Alfvén Waves To Slow Waves

Figure 5.11 demonstrates that the conversion of shear Alfvén waves to slow waves is of negligible significance in MHD cascades. GSI contains the original prediction. A modified version of the argument given there is described below. It compares the rate at which slow waves are created in a balanced cascade composed entirely of shear Alfvén waves to the rate at which the shear Alfvén cascade.

Our starting point is the Fourier transformed equation of motion for upward prop-

agating waves written in terms of Elsasser variables

$$\left(\frac{\partial}{\partial t} - i\omega(\mathbf{k})\right)\tilde{\mathbf{w}}_{\uparrow}(\mathbf{k}) =$$
$$-\ \frac{i}{8\pi^3}\int d^3k_1\, d^3k_2 \left\{\tilde{\mathbf{w}}_{\uparrow}(\mathbf{k}_1) - \hat{\mathbf{k}}\left[\hat{\mathbf{k}}\cdot\tilde{\mathbf{w}}_{\uparrow}(\mathbf{k}_1)\right]\right\}\left[\mathbf{k}\cdot\tilde{\mathbf{w}}_{\downarrow}(\mathbf{k}_2)\right]\delta(\mathbf{k}_1+\mathbf{k}_2-\mathbf{k}) \quad (6.1)$$

where $\omega(\mathbf{k}) = k_z v_A$ is the linear frequency of the shear Alfvén and slow waves. The rates of change of the amplitudes of slow and shear Alfvén waves with wavevector $\mathbf{k}$ in a cascade of pure shear Alfvén waves are given by

$$\left(\frac{\partial}{\partial t} - i\omega(\mathbf{k})\right)\tilde{\mathbf{S}}_{\uparrow}(\mathbf{k}) =$$
$$-\ \frac{i}{8\pi^3}\int d^3k_1\, d^3k_2 \left[\hat{\mathbf{s}}(\mathbf{k})\cdot\tilde{\mathbf{A}}_{\uparrow}(\mathbf{k}_1)\right]\left[\mathbf{k}_1\cdot\tilde{\mathbf{A}}_{\downarrow}(\mathbf{k}_2)\right]\delta(\mathbf{k}_1+\mathbf{k}_2-\mathbf{k}), \quad (6.2)$$

and

$$\left(\frac{\partial}{\partial t} - i\omega(\mathbf{k})\right)\tilde{\mathbf{A}}_{\uparrow}(\mathbf{k}) =$$
$$-\ \frac{i}{8\pi^3}\int d^3k_1\, d^3k_2 \left[\hat{\mathbf{a}}(\mathbf{k})\cdot\tilde{\mathbf{A}}_{\uparrow}(\mathbf{k}_1)\right]\left[\mathbf{k}_1\cdot\tilde{\mathbf{A}}_{\downarrow}(\mathbf{k}_2)\right]\delta(\mathbf{k}_1+\mathbf{k}_2-\mathbf{k}). \quad (6.3)$$

Let us compare these two rates.[1] The magnitude of $\hat{\mathbf{s}}(\mathbf{k})\cdot\tilde{\mathbf{w}}_{\uparrow}(\mathbf{k}_1)$ is smaller than that of $\hat{\mathbf{a}}(\mathbf{k})\cdot\tilde{\mathbf{w}}_{\uparrow}(\mathbf{k}_1)$ by the scale dependent anisotropy factor $\theta \sim k_z/k_\perp \ll 1$. Thus only a fraction $\theta^2(k_\perp) \ll 1$ of the energy in shear Alfvén waves is converted into slow waves as the shear Alfvén waves cascade across $k_\perp$. This accounts for the negligible production of slow waves as shown in Figure 5.11.

6.2 Dynamics Of Imbalance

The proclivity of MHD cascades for imbalance is a consequence of nonlinear interactions being restricted to collisions between oppositely directed waves.

[1] The net growth rate of shear Alfvén waves vanishes in a steady state cascade. Restricting the integral to $k_1 \le k$ yields the rate at which the amplitude of $\mathbf{A}_{\uparrow}$ grows due to the cascading of longer ($k_1 < k$) upward propagating shear Alfvén waves.

6.2.1 Forced Turbulence

Large fluctuations are observed in the energies of different wave types in simulations of forced turbulence. Nevertheless, the imbalance appears to be bounded. Figure 5.8 provides an excellent example of this behavior.

A simple dynamical model suffices to capture the essence of imbalance in forced MHD turbulence. It consists of the coupled equations

$$\frac{dE_\uparrow}{dt} = -\frac{E_\uparrow E_\downarrow^{1/2}}{L} + \Lambda, \quad \text{and} \quad \frac{dE_\downarrow}{dt} = -\frac{E_\downarrow E_\uparrow^{1/2}}{L} + \Lambda. \tag{6.4}$$

Here E denotes the energy density of the shear Alfvén waves, L the transverse outer scale, and Λ the excitation rate. The equilibrium energy density and the nonlinear cascade time scale are defined by $E_{\text{eq}} = (\Lambda L)^{2/3}$ and $t_c = L^{1/3}/\Lambda^{2/3}$.

To investigate the stability of forced balanced cascade, we set

$$E_\uparrow = E_{\text{eq}} + \Delta E_\uparrow \quad \text{and} \quad E_\downarrow = E_{\text{eq}} + \Delta E_\downarrow, \tag{6.5}$$

and then substitute these expressions into equations (6.4) to obtain

$$\frac{d\Delta E_\uparrow}{dt} = -\frac{1}{2t_c}\left(2\Delta E_\uparrow + \Delta E_\downarrow\right) \quad \text{and} \quad \frac{d\Delta E_\downarrow}{dt} = -\frac{1}{2t_c}\left(2\Delta E_\downarrow + \Delta E_\uparrow\right). \tag{6.6}$$

Assuming a time dependence proportional to e^{st}, we find eigenvalues

$$s_1 = -\frac{1}{2t_c} \quad \text{and} \quad s_2 = -\frac{3}{2t_c}. \tag{6.7}$$

This establishes the stability of the forced balanced cascade. It also shows that fluctuations associated with the s_1 eigenmode decay rather slowly. These characteristics accord well with the runs of Alfvén wave energy densities displayed in Figure 5.8.

A more sophisticated analysis would include a proper statistical treatment of forcing and an investigation of the spectrum of fluctuations.

6.2.2 Decaying Turbulence

Simulations of decaying MHD turbulence exhibit large imbalances. Thus a perturbation analysis is inappropriate. Fortunately, for $\Lambda = 0$ equations (6.4) admit an analytic solution. As is easy to verify by direct substitution, $\Delta E^{1/2} \equiv E_{\uparrow}^{1/2} - E_{\downarrow}^{1/2} = \Delta E_0^{1/2}$ is a constant, and that

$$\frac{d}{dt} \ln \left(\frac{E_{\uparrow}}{E_{\downarrow}} \right) = \frac{\Delta E_0^{1/2}}{L}. \tag{6.8}$$

Thus imbalance grows exponentially in decaying turbulence. This accounts qualitatively for the behavior seen in Figure 5.9.

Dobrowolny et al. (1980) propose the growth of imbalance in decaying MHD turbulence as an explanation for the fact that the preponderance of shear Alfvén waves in the solar wind propagate outward along the interplanetary magnetic field. Support for this proposal is provided by simulations described in Pouquet et al. (1986).

6.2.3 Axial Asymmetry

Axial asymmetry refers to the orientation of transverse fields. An example of a field aligned with the x axis is $\mathbf{w}_{\uparrow}(x, y, z) = \mathbf{w}_{\uparrow}(y, z)\hat{\mathbf{x}}$ (all fluctuations aligned with the $\hat{\mathbf{x}}$ axis). If the down Elsasser field is aligned with the same axis: $\mathbf{w}_{\downarrow} = \mathbf{w}_{\downarrow}(y, z)\hat{\mathbf{x}}$, the fields do not interact. If instead the down Elsasser field is aligned with the crossed axis: $\mathbf{w}_{\downarrow} = \mathbf{w}_{\downarrow}(x, z)\hat{\mathbf{y}}$, the fields interact strongly. These are the extreme examples, and they illustrate that energy can exist in both transverse Elsasser fields without cascading. In general, fields of all orientations will exist and the alignment will not be total as it was in the previous examples.

Unforced turbulence is unstable to the onset of axial asymmetry. Suppose that more energy is aligned with $\hat{\mathbf{x}}$ than with $\hat{\mathbf{y}}$. Let the energies in both propagation directions be equal, although this is less central to the point. The dominant alignment cascades the subdominant alignment more quickly (relative to its own energy) than

it itself is cascaded. Analogous to the phenomenon of imbalance in section 6.2.2, we expect the subdominant alignment to be eliminated leaving behind the dominant alignment. In forced turbulence, we expect the distribution of alignments to be affected by this instability. In particular, we expect that if the turbulence is preferentially aligned at some scale, the turbulence will retain this alignment as it cascades to smaller scales.

6.3 Intermittency

Tubes of high vorticity, often referred to as worms, are prominent features in simulations of hydrodynamic turbulence. Worms have diameters of order the dissipation scale and lengths approaching the outer scale. They are thought to form from the rolling up of vortex sheets. In spite of their prominence, worms do not affect the inertial range dynamics (Jiminez et al. 1993).

Coherent structures are also evident in MHD simulations. Examples are shown in §5.7 where the magnitudes of the curls of the dynamical fields and of the gradient of the passive scalar are plotted in (x, y) slices. These regions have narrow dimensions comparable to the dissipation scale and lengths approaching the outer scale $L_\perp$. In these respects they resemble worms. However, we suspect that these structures are sheets which extend along the z axis. Slices taken at different values of z appear to support this assertion, since they show correlation lengths $\Delta z \approx 0.03$. Unfortunately, this distance is smaller that the parallel dissipation scale, so the true extent of the sheets along this direction cannot be determined. We can only speculate that what we observe in the slices are cross sections of vortex sheets which the magnetic field prevents from rolling up.

6.3.1 Intermittency and Scalings

We propose an explanation for the departure from GS scalings. Self-similarity is the assumption that turbulent structure is scale independent. Collectively, the phenomena of spatial intermittency, polarization, and axial asymmetry suggest that this is

not the case. These phenomena impose extra conditions which must be satisfifed for cascading interactions to occur. Therefore, in a highly intermittent turbulence we expect the distributions of wavepacket energies and interaction strengths to become sparse. Scalings for the cascade time ($t_c \sim \lambda_\perp / v_\perp$) and critical balance ($\lambda_\parallel v_\perp \sim \lambda_\perp v_A$) may require modifiction because $v_\perp$ and $\lambda_\parallel$ are globally averaged quantities while the significant interactions occur at the sparse end of the distribution.

It is worth noting that these obstacles to cascade are not present in hydrodynamic turbulence. Even if energy is intermittently distributed, eddies will still cascade according to the local λ/v.

Our simulations are restricted to 1.5 decades of inertial range, where we observe fourth order moments of the fields with a magnitude of ~ 5 at the smallest scale. The likely result of greater range is even greater intermittency. It would be a worthy enterprise to investigate the impact of intermittency on an MHD cascade of astrophysical range.

6.4 Low-β Turbulence.

We have rigorously treated the high-β (ratio of plasma to magnetic pressure) cascade, and here we offer some qualitative observations for the low-β cascade. We assume only that fluctuations are small with respect to the Alfvén and acoustic speeds. We begin with the full MHD eigenvectors for arbitrary Alfvén and acoustic speeds v_A and v_S (Shu 1992). Define mean and fluctuating quantities as

$$b = b_0 \hat{\mathbf{z}} + b_0 (b_{\hat{a}} \hat{\mathbf{a}} + b_{\hat{s}} \hat{\mathbf{s}})\, e^{i(\mathbf{k}\cdot\mathbf{x} - \omega t)} \qquad v = (v_{\hat{k}} \hat{\mathbf{k}} + v_{\hat{a}} \hat{\mathbf{a}} + v_{\hat{s}} \hat{\mathbf{s}})\, e^{i(\mathbf{k}\cdot\mathbf{x} - \omega t)}$$

$$\rho = \rho_0 + \rho_0 \rho_1\, e^{i(\mathbf{k}\cdot\mathbf{x} - \omega t)}$$

$\hat{\mathbf{k}}$, $\hat{\mathbf{a}}$, and $\hat{\mathbf{s}}$ are the right-hand unit vectors from section (2.3) with $\cos(\psi) = \hat{\mathbf{k}} \cdot \hat{\mathbf{z}}$. The Alfvén wave dispersion relation is $\omega^2/k^2 = v_A^2 (\hat{\mathbf{z}} \cdot \hat{\mathbf{k}})$, and the eigenvectors are

$$\rho_1 : v_{\hat{a}} : b_{\hat{a}} \;=\; 0 : \pm v_A : -1.$$

The dispersion relations for the fast (+) and slow (-) modes are

$$\frac{w^2}{k^2} = \frac{1}{2}\left[(v_A^2 + v_S^2) \pm [(v_A^2 + v_S^2)^2 - 4v_A^2 v_S^2 \cos^2\psi]^{1/2}\right]$$

The eigenvectors are $\rho_1 : v_{\hat{k}} : v_{\hat{s}} : b_{\hat{s}}$

$$= \cos\psi \sin\psi : \frac{w}{k}\cos\psi\sin\psi : \frac{w}{k}\left[\sin^2\psi + \frac{v_S^2 - w^2/k^2}{v_A^2}\right] : -\frac{v_S^2 - w^2/k^2}{v_A^2}\cos\psi$$

In the limit of transverse wavevectors and low β: $v_A >> v_S$ and $\psi \to \pi/2$, the fast and slow mode dispersion relations are $\omega^2/k^2 = v_A^2 + v_S^2$ and $v_S^2\cos^2(\psi)$, and the slow mode eigenvectors are

$$\rho_1 : v_{\hat{k}} : v_{\hat{s}} : b_{\hat{s}} \;=\; 1 : \pm v_S\cos(\psi) : \pm v_S : -\frac{v_S^2}{v_A^2}$$

The slow mode is an acoustic wave constrained to propagate along fieldlines.

In the low-β cascade, magnetic pressure imposes incompressibility on Alfvén waves and we expect the dynamics of the pure Alfvén-wave cascade to be the same as for high-β turbulence. This conclusion requires only that the fluctuations be substantially smaller than the Alfvén speed. At high β, slow waves cascade Alfvén waves by altering the Alfvén speed through fluctuations in b_z. At low β, the same is accomplished through fluctuations in ρ. In both cases the effect on the Alfvén waves is suppressed by a factor of $\lambda_\perp/\lambda_{||}$. Slow waves can also cascade Alfvén waves through transverse magnetic fluctuations $\cos(\psi)b_{\hat{s}}$. Define R to be the ratio of transverse magnetic fluctuations due to slow and Alfvén waves when each have comparable energy. For low β, $R \sim v_S\cos(\phi)/v_A$ and the slow waves are not significant.

For $v_A = v_S$ and $\cos\psi \sim 0$, $R \sim \cos\psi$ and slow waves are again not significant. The fast (+) and slow (-) mode dispersion relations are $\omega^2/k^2 = v_A^2(1 \pm \sin\psi)$, and the slow mode eigenvectors are

$$\rho_1 : v_{\hat{k}} : v_{\hat{s}} : b_{\hat{s}} \;\sim\; 1 : \pm v_S\frac{1}{\sqrt{2}}\cos\psi : \pm\sqrt{2}v_S : -1.$$

6.5 Comparison With Previous Simulations

Shebalin et al. (1983) report the development of anisotropy in isotropically excited MHD. Their simulations are two-dimensional, with one axis parallel to the direction of the mean magnetic field. Thus they are composed entirely of slow waves. An isotropic distribution of slow waves will initiate an anisotropic cascade. However, nonlinear interactions among slow waves weaken as the cascade becomes more transverse because their strength is proportional to coefficients such as $\mathbf{k}_2 \cdot \mathbf{S}_{\downarrow}(\mathbf{k}_1)$, and for $\mathbf{k} \rightarrow \mathbf{k}_{\perp}$, $\hat{\mathbf{s}} \rightarrow \hat{\mathbf{z}}$.[2] Convincing demonstrations of the development of anisotropy in fully three-dimensional MHD simulations are presented in Oughton et al. (1994) and in Matthaeus et al. (1998). Each of these papers provides evidence that anisotropy increases at smaller scales. Each also claims that up to a saturation limit, anisotropy is more pronounced the larger the ratio of mean to fluctuating magnetic field strength. Matthaeus et al. note that this latter trend is inconsistent with the scaling for anisotropy proposed by GSI.

An analysis by Cho & Vishniac (2000) clears up the confusion regarding the scale dependence of anisotropy in MHD turbulence. Unlike previous workers, who measure anisotropy in coordinate systems fixed to the sides of their computational boxes, Cho and Vishniac compute anisotropy in local coordinate frames tied to the direction of the total magnetic field. We apply a similar technique of using structure functions computed in directions parallel and perpendicular to that of the local magnetic field in our own study of anisotropy (see §5.2.1). Both they and we find results that are consistent with the relation $\lambda_{||} \propto \lambda_{\perp}^{2/3}$ proposed by GSI. The difference between our simulations and Cho and Vishniac's is that the ratio of fluctuating to mean fields is ~ 0.01 in ours and is ~ 0.5 in theirs

[2] This remains true in 3D

6.6 Acknowledgements

We wish to thank Steven Cowley, Yoram Lithwick, Eugene Chiang, Eric Blackman, Benjamin Chandran, Andrew Melatos, and Reuben Krasnopolsky for useful discussions. Most of all JM would like to thank Peter Goldreich, the advisor for the thesis. The supercomputers used for these simulations are operated by the Caltech Center for Advanced Computing Resources and their very helpful staff, especially Edith Huang. JM is supported by an NSF Graduate Research Fellowship and the Caltech Physics and Astronomy Department TA industry.

Bibliography

[1] Armstrong, J. W., Rickett, B. J., & Spangler, S. R. 1995, ApJ, 443, 209

[2] Blandford, R., & Eichler, D., 1987, Phys. Reports, 154, 1

[1988] Canuto, C. 1988, Spectral Methods In Fluid Dynamics (Berlin:Springer-Verlag)

[3] Chandran, B., Cowley, S., "Thermal Conduction in a Tangled Magnetic Field", PRL V80, no. 14, 1998

[4] Chandran, B.D.G., 2000, PRL, in press

[2000] Cho, J. & Vishniac, E.T. 2000, ApJ, 539, 273

[1980] Dobrowolny, M., Mangeney, A. & Veltri, P. 1980, Phys. Rev. Lett., 45, 144

[5] Dyson, J.E., & Williams, D.A., 1997, "The Physics of the Interstellar Medium" (Institute of Physics Publishing)

[1995] Goldreich, P. & Sridhar, S. 1995, ApJ, 438, 763

[1997] Goldreich P. & Sridhar, S. 1997, ApJ, 485, 680

[6] Heiles, C., Presented at the 4th Tetons summer conference: "Galactic structure, stars, and the interestellar medium."

[1963] Iroshnikov, P.S. 1963, AZh, 40, 742

[1993] Jimenez, J., Wray, A.A., & Saffman, P.G. 1993, J. Fluid Mech., 255, 65

[1941] Kolmogorov, A.N. 1941, Dokl. Akad. Nauk SSSR, 30, 9

[7] Kraichnan, R.H., 1965, Phys. Fluids, 8, 1385

[8] Kulsrud, R., & Pearce, W., 1969, ApJ, 156, 445

[1990] Lesieur, M. 1990, "Turbulence In Fluids" (Dordrecht:Kluwer)

[9] MacLow, M, McCray R, Norman ML, ApJ 337, 141, 1989

[1998] Matthaeus, W.H., Oughton, S., Ghosh, S., & Hossain, M. 1998, PRL, 81, 2056

[10] Minter, A. H., & Spangler, S. R. 1996, ApJ, 458, 194

[11] Molnar, L. A., Mutel, R. L., Reid, M. J., & Johnston, K. J. 1995, ApJ, 438, 708

[1996] Ng, C.S. & Bhattacharjee, A. 1996, ApJ, 465, 845

[1994] Oughton, S., Priest, E.R., & Matthaeus, W.H. 1994, J. Fluid Mech., 280, 95

[1979] Parker, E.N. 1979, Cosmical Magnetic Fields (Oxford:Oxford Univ. Press)

[1986] Pouquet, A., Meneguzzi, M. & Frisch, U. 1986, Phys. Rev. A, 33, 4266

[1983] Shebalin, J.V., Matthaeus, W.H. & Montgomery, D.J.J. 1983, J. Plasma Phys., 29, 525

[12] Shu F. H., "The Physics of Astrophysics Volume II: Gas Dynamics", 1992

[13] Spangler, S. R. & Cordes, J., ApJ, 505, 766, 1998

[14] Spitzer, "Physical Processes in the Interstellar Medium", 1978

[1994] Sridhar S. & Goldreich, P. 1994, ApJ, 432, 612

[15] Wakker BP, van Woerden H, ARAA 1997

Chapter 7 APPENDIX

7.1 Code

The spectral code is divided into files having the following functions:

bleys.f	Top level shell. Calls bleys_rk.f.
bleys_rk.f	The Runge-Kutta timestep engine.
prime_mpi2.f	Evaluate the time derivative of the fields.
bleys_util.f	Utilities.
force.f	Forcing subroutines.
fftjlm_mpi.f	3D MPI-parallel FFT. Contains the transpose subroutines.
fftjlm_bleys.f	Portal to select the correct 1D FFT array size.
fftjlm_p00256.f	Pseudo-assembly language 1D FFT, 256 elements, e^{+ikx}.
fftjlm_m00256.f	Pseudo-assembly language 1D FFT, 256 elements, e^{-ikx}.
fftjlm_p00128.f	Pseudo-assembly language 1D FFT, 128 elements, e^{+ikx}.
fftjlm_m00128.f	Pseudo-assembly language 1D FFT, 128 elements, e^{-ikx}.
prime_ehd.f	Compute the electron hydrodynamics (EHD) terms.
slow.f	Selectively damp slow modes, if specified.
viscosity.f	Anisotropic tensor viscosity for use with the turbulent dynamo.
io.in	Input parameters read by the program during execution.
bleys.e	The executable.

The contents of bleys_rk.f constitute the engine that organizes the Runge-Kutta algorithm and utility calls. Its structure is as follows:

Set default parameters and read input parameters from disk.

Read real-space fields from disk and transform to Fourier space.

Write a record of the parameters used for future reference.

Begin timestep loop.

Read changeable parameters from disk, such as savetimes.

Write fields to disk in real space, if specified.

Halt execution, if specified.

Implement forcing, if specified.

Dealias.

Compute the time derivative of the fields.

Compute the first Runge-Kutta trial. This includes viscosity.

Dealias.

Compute the time derivatives of the fields from the first RK trial.

Compute the final Runge-Kutta step.

End timestep loop.

prime_mpi2.f Computes the time derivative of $\mathbf{v}$, $\mathbf{b}$, and n. The procedure minimizes the number of FFTs computed and memory allocated. It has the following structure.

Input: $\tilde{\mathbf{v}}$, $\tilde{\mathbf{b}}$, and $\tilde{n}$, real and imaginary parts (14 arrays).

Output: $\partial_t\tilde{\mathbf{v}}$, $\partial_t\tilde{\mathbf{b}}$, and $\partial_t\tilde{n}$, real and imaginary parts, stored in input arrays.

Work arrays: $\mathbf{v}$ and $\mathbf{b}$ in real space (6 arrays), zr and zi for FFTs (2 arrays).

Procedure:

Transform to real space: $\tilde{\mathbf{v}}, \tilde{\mathbf{b}} \longrightarrow \mathbf{v}, \mathbf{b}$.

$\tilde{\mathbf{v}}$ and $\tilde{\mathbf{b}}$ are now free. The terms comprising $\partial_t\tilde{\mathbf{v}}$ and $\partial_t\tilde{\mathbf{b}}$ will be summed here.

Compute the tensor viscosity if specified.

Compute each component of $v_iv_j - b_ib_j$, transform to Fourier space, sum in $\partial_t\tilde{\mathbf{v}}$.

Compute each component of $v_ib_j - v_jb_i$, transform to Fourier space, sum in $\partial_t\tilde{\mathbf{b}}$.

Compute the EHD terms if specified.

Transform $\tilde{n}$ to real space and store in $\tilde{n}$.

Compute each component of v_in, transform to Fourier space, store in $\mathbf{v}$ and $\mathbf{b}$.

Sum the results and store in $\tilde{n}$, which is now $\partial_t\tilde{n}$.

Multiply $\tilde{\mathbf{v}}, \tilde{\mathbf{b}}, \tilde{n}$ by the Fourier normalization $(n_1n_2n_3)^{-1}$.

bleys_util.f Contains the following utilities:

subroutine alias: Perform the dealiasing truncation.

subroutine advance: Timestep with viscosity included by an integrating factor.

subroutine matrixbuild: Compute matrix product A = B*C + D*E.

subroutine cache: Copy 1D segments from 3D arrays, vital for cache utilization.